Design and Simulation of a Refractive Index Sensor Based on SPR and LSPR using Gold Nanostructures

Armin Agharazy Dormeny

A Thesis

In the Department

Of

Electrical and Computer Engineering

Presented in Partial Fulfillment of the Requirements
For the Degree of
Master of Applied Science (Electrical Engineering) at
Concordia University
Montreal, Quebec, Canada

April 2020

CONCORDIA UNIVERSITY

SCHOOL OF GRADUATE STUDIES

This is to certify that this thesis is prepared

By: Armin Agharazy Dormeny

Entitled: Design and Simulation of a Refractive Index Sensor Based on SPR and LSPR using Gold Nanostructures

and submitted in partial fulfillment of the requirements for the degree of

Master of Applied Science (Electrical and Computer Engineering)

complies with the regulations of the University and meets the accepted standards with respect to originality and quality.

Signed by the final examining committee:

_____ Chair
Dr. Steve Shih

_____ External Examiner
Dr. Javad Dargahi

_____ Examiner
Dr. Steve Shih

_____ Thesis Supervisor
Dr. Mojtaba Kahrizi

Approved by

Dr. Rastko Selmic, Graduate Program Director

April 2020 _____

Dr. Amir Asif, Dean
Gina Cody School of Engineering & Computer Science

Abstract

Design and Simulation of a Refractive Index Sensor Based on SPR and LSPR using Gold Nanostructures

Armin Agharazy Dormemy, MASc.
Concordia University, 2020

In the last two decades, the unusual optical and physical properties of novel metallic nanostructures (such as gold, silver, and aluminum) has been the subject of intense research efforts. Surface plasmon resonance and localized surface plasmon resonance are two of the unique phenomena in novel metals which can be used to create different kinds of sensitive sensors and biosensors.

In this work, a refractive index sensor based on surface plasmon resonance is designed and analytically investigated by a finite element method via COMSOL Multiphysics to detect chemicals. The intensity, spectral width and sensitivity of the plasmonic signals are highly affected by the shape, size, and configuration of the metallic nanostructures. Patterning the planar metallic thin film with cavities or protrusion can result in obtaining a tunable sensitivity for the sensor. The architecture of the nanohole/nanowire arrays leads to a nanostructure having multiple plasmonics properties.

The simulation results show that the co-excitation of surface plasmon resonance and localized surface plasmon resonance modes can enhance the sensitivity of the SPR-based sensors significantly. To obtain this result, several cut lines through the metallic thin film were considered and the variation of the electric field intensity along those cut lines is studied. To determine the SPR and LSPR modes, the penetration depth of the plasmon field is characterized at metal/dielectric interfaces.

After investigation of three models for the metallic layer (planar thin film, nanohole patterned thin film, and protrusive thin film), it was concluded that the device made of 20 nm cylindrical nanowire supported by a 40 nm thin film can result in the best performance parameters (in terms of sensitivity, absorption, and accuracy). Eight substances with refractive indices ranging from 1.333 to 1.38 were used to obtain the calibration data of the optimum sensor. The linear characteristic of the calibration curve shows that the sensor is able to detect unknown materials as a function of resonance wavelength. This study is proposing a new way to show the duality nature of patterned thin films to support both propagating and localized surface plasmon modes.

Acknowledgements

First and foremost, I would like to express my sincere gratitude to my supervisor Dr. Mojtaba Kahrizi for the continuous support of my study and research, for his patience, assistance, enthusiasm, and immense knowledge. His guidance helped me in all the time of research and writing this thesis. Without his advices, guidance and patience this thesis wouldn't reach its present form.

Moreover, I would like to express my gratitude to Dr. Parsoua Abedini Sohi, my great colleague in "Nanotechnology" group, who had acted as an equal supervisor for me. During my masters, she has always answered my questions with patience and helped me through difficulties of the research.

I would like to convey my heartfelt thanks to Concordia University for offering me an environment to study and concentrate on my thesis. I have enjoyed the company of my friends; Yatexu, Mehrnegar, Morvarid, Saman, Farinaz, and Dmytry. I wish to thank them all for their friendship and support.

Finally, I must express my very profound gratitude to my Parents, for providing me with unfailing support and invaluable care not only during my years of study but also throughout my whole life. Definitely this accomplishment would not have been possible without them.

Many thanks to all of you!

Armin Agharazy Dormeny

List of Publications and Conference Contributions

1. Armin Agharazy Dormeny, Parsoua Abedini Sohi, and Mojtaba Kahrizi. "Design and simulation of a refractive index sensor based on SPR and LSPR using gold nanostructures." Results in Physics 16 (2020): 102869.
2. Armin Agharazy Dormeny, Dmytry Grudin, Parsoua Abedini Sohi, Mojtaba Kahrizi. "Development of low voltage gas ionization tunneling sensor based on p-type ZnO nanostructures." Sensors and Actuators A: Physical 299 (2019): 111627.[1]
3. Armin Agharazy Dormeny, Parsoua Abedini Sohi, and Mojtaba Kahrizi. "On the sensitivity of optical fiber surface plasmon resonance based sensor for detection of dielectric analytes using COMSOL Multiphysics." 2019 International Conference on Numerical Simulation of Optoelectronic Devices (NUSOD). IEEE, 2019.
4. Armin Agharazy Dormeny, Dmytry Grudin, Parsoua Abedini Sohi, Mojtaba Kahrizi. "Development of gas ionization tunneling sensor based on silver doped ZnO nanostructures." Poster Presentation at 2019 ECE Graduate Student Research (GSR) Conference, Concordia University, March 2019.

1- Discussed in Appendix I

To my parents

TABLE OF CONTENTS

LIST OF FIGURES

LIST OF TABLES

LIST OF ACRONYMS

ATR	Attenuated Total Reflection
EDXS	Energy-dispersive X-ray Spectroscopy
EOT	Extraordinary Optical Transmission
FEM	Finite Element Method
FOM	Figure of Merit
FPBC	Figure Periodic Boundary Condition
FWHM	Full Width at Half Maximum
GFITS	Gas Field Ionization Tunneling Sensors
GIS	Gas Ionization Sensors
GIBS	Gas Ionization Breakdown Sensors
IB	Inter-Band
IR	Infrared
LSPR	Localized Surface Plasmon Resonance
NP	Nanoparticle
RI	Refractive Index
SEM	Scanning Electron Microscope
SERS	Surface-Enhanced Raman Spectroscopy
SP	Surface Plasmon
SPP	Surface Plasmon Polariton
SPR	Surface Plasmon Resonance
TEM	Transmission Electron Microscope
TIR	Total internal reflection
TM	Transverse Magnetic
UV	Ultra Violet

LIST OF SYMBOLS

θ	Angle of incidence	[degree]
θ_{sp}	Resonance angle	[degree]
β	Wave vector of the surface plasmons	------
ε_0	Dielectric function	------
ε_m	Dielectric function of the metallic medium	------
ε_d	Dielectric function of the dielectric medium	------
ε_S	Dielectric function of the sensing medium	------
k_0	Propagation constant of light	[m^{-1}]
ω_p	Plasma frequency	[rad/s]
N	Concentration of free electrons	[m^{-3}]
e	electron charge	[C]
m_e	electron mass	[Kg]
L	propagation length	[m]
δ	penetration depth	[m]
δ_m	propagation depth of the metallic medium	[m]
δ_d	propagation depth of the dielectric medium	[m]
θ_{sp}	Resonance angle	[degree]
d_m	Thickness of the metallic film	[m]
r_{pm}	Reflection coefficient of the silica/metal layer	------
r_{ms}	Reflection coefficient of the metal/air layer	------
a	radius of the nanoparticle	[m]
χ	Shape factor	------
λ	Wavelength	[m]
n	Refractive index of material	------
ω	Frequency of the light	[Hz]
$\varepsilon_r + i\varepsilon_i$	Complex dielectric function of nanoparticle	------

M	Number of particles	------
$E(\lambda)$	Extinction cross-section of nanoparticle	------
R	Reflectivity	------
k_x	Wave vector at x direction	[m^{-1}]
k_F	Wave vector at Floquet boundary condition	[m^{-1}]
k_{jz}	Wave vector at z direction	[m^{-1}]
k_{sp}	Wave vector of surface plasmon	[m^{-1}]

Chapter 1
Introduction

1.1 Nanotechnology Enabled Sensors

Sensors based on nanostructures are becoming widely used in numerous fields such as medical diagnosis, environmental monitoring, chemical and petrochemical industries, food and drink processing, and industrial productions [1]-[3]. Low cost, reversibility, sensitivity, fast response time, durability, high resolution, online monitoring, and low power are among the most important requirements for ideal sensors. Although achieving a sensor with all the mentioned properties is very hard, but with the help of nanotechnology, many sensors have been developed to satisfy different needs of industry by employing different sensing mechanisms. Considering the transduction mechanisms, we can classify sensors into six different categories: (1) optical sensors, (2) electrochemical sensors, (3) electrical sensors, (4) mass-sensitive sensors, (5) calorimetric sensors, and (6) magnetic sensors [4].

Among these methods, optical sensors have gained much attention among researchers because of their low cost of fabrication, high speed, compactness, and the ability of real-time analysis. Fluorescence, absorption, colorimetry, Raman, refractive index (RI), surface plasmon resonance (SPR), and luminescence are the main sensing mechanisms used in optical sensing methods [5]. Surface plasmon resonance-based optical sensors have evolved as highly versatile and valuable sensing tools as a label-free approach with high sensitivity. SPR is the collective resonance of conduction electrons oscillating at the interface of materials with negative and positive permittivity, i.e., metal and a dielectric material, stimulated by the p-polarized light on a certain wavelength [6]. Kretschmann configuration, Otto configuration, and fiber optic approach are the

three main ways for utilizing SPR. The first two methods are prism-based, and consequently, they are too bulky and not suitable for remote sensing. In addition to the mentioned privileges, other advantages like narrower resonance peaks with high sensitivity and tunability have turned the fiber approach into an attractive way for sensing applications [7].

1.2 Brief History

Since the first demonstration of surface plasmon resonance, in the early 1980s, the technology and application of SPR sensors have been greatly improved. Due to the tunability of the optical properties of metallic nanostructures, these types of sensors have been extensively used for biosensing, surface-enhance Raman spectroscopy (SERS), chemical sensing, bioimaging, etc. However, SPR was being used in some of the outstanding artworks from a long time ago. The Lycurgus cup (dating from the 4th century A.D.) is one of the most famous examples. This cup (as shown in figure 1.1) shows a green color when it is illuminated from outside and observed with reflected light and shines in red when it is illuminated from inside in transmitting light conditions. Moreover, as shown in figure 1.2, from the artworks that remained from the medieval periods, one can understand that the artists have had good knowledge about the optical properties of metallic nanoparticles to induce different colors in the stained-glass windows in churches and cathedrals [8].

Figure 1. 1 (Adopted from British Museum Database [9]) "Lycurgus cup dating from the 4th century A.D. The glass appears green when illuminated from the outside and purple-red when illuminated from the inside."

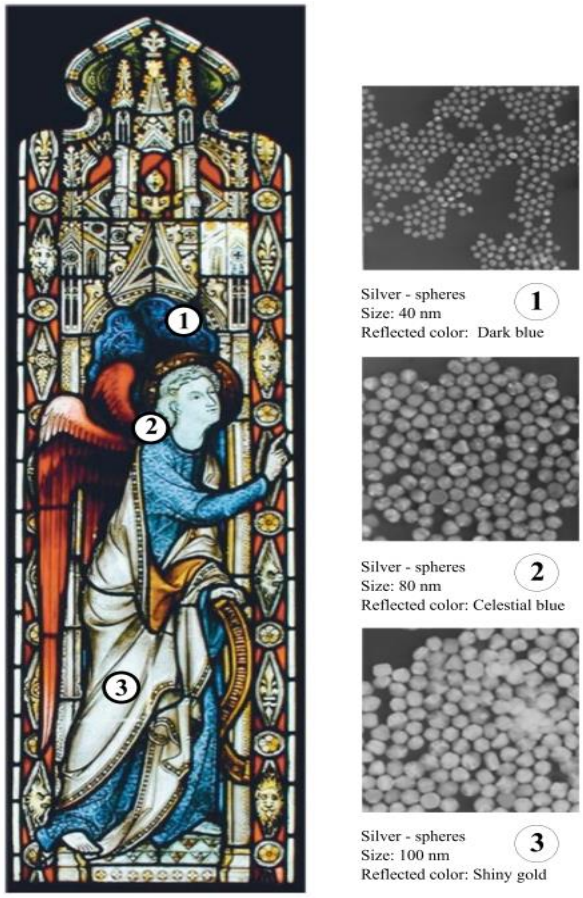

Figure 1. 2 (adopted from Chang [10]) "Use of nanoparticles with different sizes to create different colors in the stained-glass windows."

1.3 Basic Knowledge of SPR and LSPR

1.3.1 Surface Plasmon Resonance in metallic thin films

As electromagnetic waves, surface plasmons (SPs) are transverse magnetic (TM), and as a result, they need p-polarized light for excitation. The amplitude of the electric field associated with a SP wave is maximum at the metal/dielectric interface and decays exponentially in metal as well as in dielectric [11]. By solving Maxwell equations, it is found that the oscillations of SPs are

supported at the interface between the materials with positive dielectric constant and the materials with negative dielectric constants such as gold (Au), Silver (Ag) and aluminum (Al) [12]. Moreover, to satisfy the boundary conditions, we should have $|\varepsilon_m| < \varepsilon_d$ where ε_m and ε_d are symbolizing the wavelength dependent dielectric constants of metal and dielectric, respectively. The wave vector of light with a wavelength of λ traveling with angle θ toward the surface of a medium with dielectric constant ε_0 is defined as:

$$\mathrm{k}_x = \frac{2\pi}{\lambda}\sqrt{\varepsilon_0}\ \sin\theta \tag{1}$$

To excite surface plasmons, the wave vector of the electric field component of the light at the surface ($\mathbf{k}_x$) should be along the direction of wave vector of the surface plasmon (β) which results in the dispersion relation for surface waves:

$$\beta = k_x = k_0\sqrt{\left(\frac{\varepsilon_d\varepsilon_m}{\varepsilon_d+\varepsilon_m}\right)} = \frac{2\pi}{\lambda}\sqrt{\left(\frac{\varepsilon_d\varepsilon_m}{\varepsilon_d+\varepsilon_m}\right)} \tag{2}$$

where k_0 describes the propagation constant of the incident light. In other words, at resonance condition, the frequency of the incident light matches the frequency of the electrons oscillations at the metal surface [13].

To match the wave vector of SPs to that of the incident light, the wave vector of the light should be changed. For that, the most common way is to use a dielectric material with n > 1 for passing the light, and as a result, dispersion relations of the SPs and the evanescent field of the incident light will intersect each other [14].

Considering the absorption, an imaginary part is introduced to the permittivity of metals which allows the existence of guided modes even for $|\varepsilon_m| > \varepsilon_d$. Rewriting the propagation constant of SPs in the complex form, when the magnitude of the real part of the metal's dielectric function is much greater than its imaginary part ($|\varepsilon'_m| \gg \varepsilon''_m$) results in:

$$\beta = \beta' + i\,\beta'' = \frac{2\pi}{\lambda}\sqrt{\left(\frac{\varepsilon_d \varepsilon'_m}{\varepsilon_d + \varepsilon'_m}\right)} + i\frac{2\pi}{\lambda}\frac{\varepsilon''_m}{2(\varepsilon'_m)^2}\left(\frac{\varepsilon_d \varepsilon_m}{\varepsilon_d + \varepsilon_m}\right)^{\frac{3}{2}} \quad (3)$$

The imaginary part of the metal's dielectric function leads to an imaginary part in the propagation constant of SPs. β'' is associated with the attenuation of the SPs which is usually characterized by the propagation length (L) which is defined as the distance in the direction of propagation at which the energy of the SP decreases by a factor of 1/e:

$$L = \frac{1}{2\beta''} \quad (4)$$

When a p-polarized light is incident on the interface of the metal/dielectric, a part of the light gets reflected into the dielectric medium, and a part gets transmitted into the metal as an inhomogeneous electromagnetic wave. This is referred to as the evanescent wave, which decays exponentially. The evanescent wave gets coupled with the SP wave when the propagation constants of both waves are equal, and it excites the SPs [15]. Penetration depth (δ) of the evanescent field defines the distance from the interface at which the amplitude of the evanescent field decreases by a factor of 1/e. The electromagnetic field is maximum at the interface of metal and dielectric and decays exponentially in a direction normal to the interface and is calculated from the following equation [16]:

$$\delta_m = \frac{\lambda}{2\pi}\sqrt{\left|\frac{\varepsilon_d + \varepsilon_m}{{\varepsilon_m}^2}\right|} \quad \text{and} \quad \delta_d = \frac{\lambda}{2\pi}\sqrt{\left|\frac{\varepsilon_d + \varepsilon_m}{{\varepsilon_d}^2}\right|} \quad (5)$$

From equation 5, it can be concluded that the decay of the electric field into the metal is much shorter than the decay into the dielectric, as shown in figure 1.3, and by increasing the wavelength of the incident light, penetration depth increases. The penetration depth into the metallic layer is in the order of tens of nanometers, although it is in the order of half a wavelength in the dielectric medium [17].

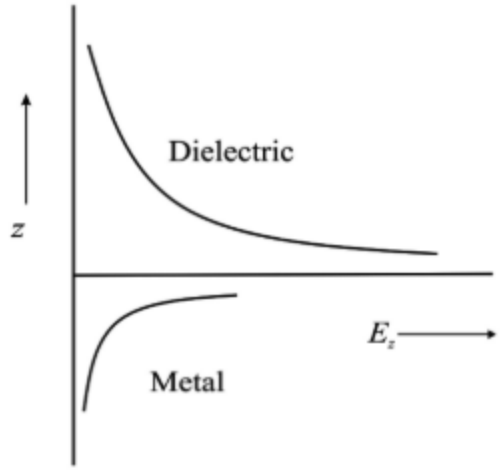

Figure 1. 3 (adopted from Nivedha [18]) "Exponential decay of field intensity of surface plasmon mode in a metal and dielectric system."

When the evanescent wave excites the SPs, the energy from the incident light transfers to the SPs, which results in the reduction of the energy of the reflected light. As a result, by measuring the normalized reflected intensity (R) as a function of wavelength of the light or incident angle, a sharp dip is observed at resonance angle, θ_{sp}, due to an efficient transfer of energy to SPs. However, the position and sharpness of the dip are highly dependent on the thickness of the metallic layer. In small thicknesses, the electron oscillations are damped due to the confinement effects, and as a result, we cannot observe sharp dips in the spectra.

On the other hand, when the thickness of the metal gets larger than a certain value (usually more than 70 nm), the dip becomes smoother as the evanescent field of the incident light reaching the other side of the metallic film is very weak. Another issue with the thickness of the metal is the ability of the sensor to differentiate between the changes in the refractive index of its environment. When the metal layer is too thick, since the evanescent field cannot reach the other side of the film, the sensor is completely insensitive to the changes of the refractive index of its surrounded media.

Moreover, when the metallic film becomes too narrow, because of the confinement effects and low electron concentration, an appropriate differentiation between refractive index changes by the sensor cannot be observed. As a conclusion, one can say that the value of R depends on the combination of incident light frequency, angle of incidence, and the thickness of the metal layer.

Fresnel's equations can give the quantitative description of the minimum of the reflected intensity R for the three-layer system p/m/s. Where "p" stands for high refractive index material, e.g., fused silica, "m" stands for the metal film with thickness "d_m", and "s" stands for low index dielectric medium, e.g., air, water, etc. The reflectivity R for p-polarized light is given by [12], [16]:

$$R=\left|\frac{r_{pm}+r_{ms}e^{2ik_{mz}d_m}}{1+r_{pm}r_{ms}e^{2ik_{mz}d_m}}\right|^2 \tag{6}$$

where $r_{pm}\ and\ r_{ms}$ are the amplitude of reflection coefficients for the silica/metal layer and metal/air layer, respectively and are obtained from the following relationships:

$$r_{pm}=\frac{k_{pz}\varepsilon_m-k_{mz}\varepsilon_d}{k_{pz}\varepsilon_m+k_{mz}\varepsilon_d} \quad \text{and} \quad r_{ms}=\frac{k_{mz}\varepsilon_s-k_{sz}\varepsilon_m}{k_{mz}\varepsilon_s+k_{sz}\varepsilon_m} \tag{7}$$

where ε_m and ε_s are the dielectric constants of metallic and low index dielectric medium, accordingly and k_{jz} is the wave propagation vector in the z-direction, i.e., perpendicular to the interface in the medium j, which is calculated from:

$$k_{jz}=\sqrt{\left(\varepsilon_j\frac{4\pi^2}{\lambda^2}-{k_x}^2\right)} \tag{8}$$

and k_x is obtained from equation 1.

The wavelength dependence of the dielectric function of the fused silica is given by the Sellmeier equation below:

$$\varepsilon_s=1+\frac{a_1\lambda^2}{\lambda^2-{b_1}^2}+\frac{a_2\lambda^2}{\lambda^2-{b_2}^2}+\frac{a_3\lambda^2}{\lambda^2-{b_3}^2} \tag{9}$$

where $a_1 = 0.696749,\ a_2 = 0.408218,\ a_3 = 0.890815,\ b_1 = 0.0690660\ (\mu m),\ b_2 = 0.115662\ (\mu m),\ b_3 = 9.900559\ (\mu m)$ [19].

1.3.2 Surface Plasmon Resonance in metallic nanoparticles

When light is incident on a nanoparticle with a size that is much smaller than the wavelength of the incident light, as shown in figure 1.4, the electromagnetic field of the light exerts a force on the conduction electrons moving them towards the nanoparticle's surface. Accordingly, it results in the displacements of the electron gas with respect to their equilibrium position around positively charged ions. As a result, a negative charge is accumulated on one side and a positive charge in the opposite, creating an electric dipole [20], [21].

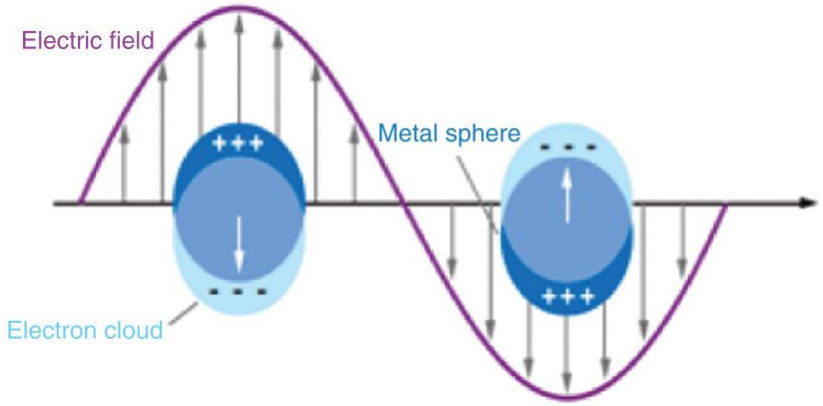

Figure 1. 4 (adopted from Szunerits [22]) "Displacements of the electron gas due to the applied electromagnetic field in metallic nanoparticles."

The displacement of the electron gas results in resonance in the oscillation frequency of electrons called resonant frequency. Similar to any other linear oscillator system, when an alternating exterior force is applied to the system, the system oscillates with the same frequency as the external force, but the amplitude and phase will depend on both the force and the intrinsic parameters of the oscillator. At the resonant frequency, the oscillating amplitude is maximum, and

the scattering processes lead to damping the electrons' movements in the nanoparticles. Therefore, same as the metallic thin films, when the frequency of the incident light matches the resonant frequency of the electrons inside the nanoparticle, an absorption band can be observed in the optical spectrum associated with the surface plasmons [23], [24].

The electromagnetic field extinction (the sum of absorption and scattering cross-sections) and the resonant frequency of metallic nanoparticles are highly dependent on the shape, size, periodicity, and type of the metal. The extinction cross-section ($E(\lambda)$) of a nanoparticle in the electrostatic dipole regime can be written as:

$$E(\lambda) = \frac{24\,\pi^2 M a^3 \varepsilon_d^{3/2}}{\lambda \ln 10}\left(\frac{\varepsilon_i}{(\varepsilon_r + \chi\varepsilon_d)^2 + \varepsilon_i^2}\right) \quad (10)$$

Where λ is the wavelength of the incident light, a is the radius of the nanoparticle, ε_d is the dielectric constant of the surrounding medium, $\varepsilon_r + i\varepsilon_i$ is the complex dielectric function of the nanoparticle, M refers to the number of particles, and χ is the shape factor, which is 2 in the case of spherical nanoparticles, and it can increase up to 20 for high aspect ratio nanostructures [25], [26].

Therefore, the position and value of the maximum absorption peak in the case of LSPR depend on many parameters like particle size, inter-particle distance, shape of the nanoparticles, composition of the nanoparticles, and refractive index of the sensing medium..

By comparing the decay length of the electric field in the case of SPR and LSPR (based on equation 4), one can see that the decay length in SPR is 15~25% of the light's wavelength. However, the decay length of LSPR based sensors is around 1~3% of the light's wavelength and depends on the size, shape, composition of the nanoparticles as well [27]. As a result, applying

metallic nanostructures rather than using thin films results in generating localized surface plasmon resonance (LSPR) which is more sensitive to local refractive index surrounding the nanostructures, it is often used to detect molecular absorption on the surface of a material. LSPR results in non-propagating surface plasmon resonance as the excitation is confined to the volume of nanoparticles with a size much smaller than the photon wavelength. On the other hand, utilizing metallic thin films can result in higher sensitivity to the bulk refractive index, lower cost of fabrication, and a lower number of parameters affecting the sensor performance [28].

1.3.3 Surface Plasmon Resonance in complex metallic nanostructures

Utilizing complex nanostructures that benefit from the combination of localized and delocalized surface plasmons (SPs) (such as micro/nano-patterned thin films) can enhance the device performance. The sensitivity of the device can be tuned by changing the periodicity, size, and shape of the structures [29], [30]. Nanovoid/Nanohole arrays, protrusive thin films, and thin film gratings are the most famous examples of complex metallic nanostructures used in SPR based sensors. Although increasing the complexity of the nanostructures from 1D (in the case of LSPR) to 2D (in the case of complex nanostructures) increases the complexity of the plasmonic properties, however, since these structures can lead to the co-excitation of both SPR and LSPR modes, they result in the further enhancement of the surface plasmon field [31].

1.4 Objective of the Research

Although various SPR/LSPR sensors exist for different applications, development of new sensitive and high-resolution SPR/LSPR sensors requires a deep understanding of the physics of these phenomena. Moreover, since obtaining a high-resolution and sensitive sensor based on

SPR/LSPR using experimental procedure can be costly and time-consuming, developing an analytical way to simulate surface plasmon resonance can help the development and optimization of these types of sensors greatly.

The goal of this research is to simulate surface plasmon resonance in complex nanostructures using the finite element method (FEM). To achieve this goal, a refractive index sensor based on SPR/LSPR has been designed and simulated using the nanostructures of gold in COMSOL Multiphysics (wave optics module).

Three models of planar thin film, perforated thin film, and protrusive thin film were designed, and the performance of the sensor has been investigated in terms of sensitivity, full width at half maximum (FWHM), and figure of merit (FOM). Moreover, the physics of SPR and LSPR in complex nanostructures in terms of the decay length of the magnified electric field at each boundary has been studied. In the end, a user-friendly environment in *COMSOL Application Builder* was developed to help to share this simulation with other researchers to design and simulate their own sensor based on the parameters such as the thickness of the thin film, size of the nanostructures, periodicity of the nanostructures, incidence angle of light, etc.

1.5 Organization of the thesis

There are five chapters in this dissertation which are organized in the following format:

Chapter II briefly describes the available platforms to create SPR/LSPR sensors to detect different kinds of materials. The advantages and drawbacks of each of the platforms and their differences are explored.

In chapter III, the model design and the simulation results for the different types of nanostructures are thoroughly discussed. The performance analysis of the modeled sensors to detect liquids and gasses is studied in this chapter,

In chapter IV the optimum design of the nanostructures for SPR/LSPR refractive index sensor is determined and its calibration data are provided. Moreover, the details about the developed application for simulating SPR is discussed in this chapter.

In chapter V, conclusions are summarized, and suggestions for future research are given.

The other contribution of the author in the development of low voltage gas ionization tunneling sensors using ZnO nanostructures is explained in Appendix I.

Chapter 2
Literature Review: SPR/LSPR Excitation Configurations

2.1 Classification of Sensing Methods

Based on the operation principles, sensors can be classified into two major groups of physical and chemical sensors. In chemical sensors, the change in the resulting data can be obtained by a chemical reaction between the sensing medium and the sensor. As a result, irreversibility, and high dependency on the pressure, moisture, and temperature of the sensing material are the main drawbacks of these types of sensors. On the other hand, physical sensors work based on a physical reaction between the sensing material and the sensor, such as electron tunneling, light absorption, etc. Therefore, they have overcome the disadvantages of the chemical sensors [32], [33]. SPR based sensors are physical sensors that work based on the interaction of the incident electromagnetic wave with the surface electrons of a highly conductive metal. The following sections describe different platforms for the utilization of SPR in sensors.

2.2 Excitation of Surface Plasmons

Utilizing electrons or light are the main methods to excite SPs. However, approaches that use light to excite SPs are more affordable, and they have been explored more frequently [34]. As discussed in the previous chapter, to excite surface plasmons, the wave vector of the incident light at the interface of the metallic nanostructure and the sensing medium, should match with the wave vector of the SPs. As shown in figure 2.1, since for the same energy, SPs have a greater wave vector compared to the incident light, they cannot be excited when the light is illuminated

directly from the air, and the wave vector of the light should be augmented using some mediocre media (with a refractive index of n > 1, such as a glass) or by changing the configuration of the metallic nanostructure. As a result, various experimental techniques have been developed to provide the necessary wave vector conservation such as prism coupling, grating coupling, waveguide coupling, etc [35]-[40].

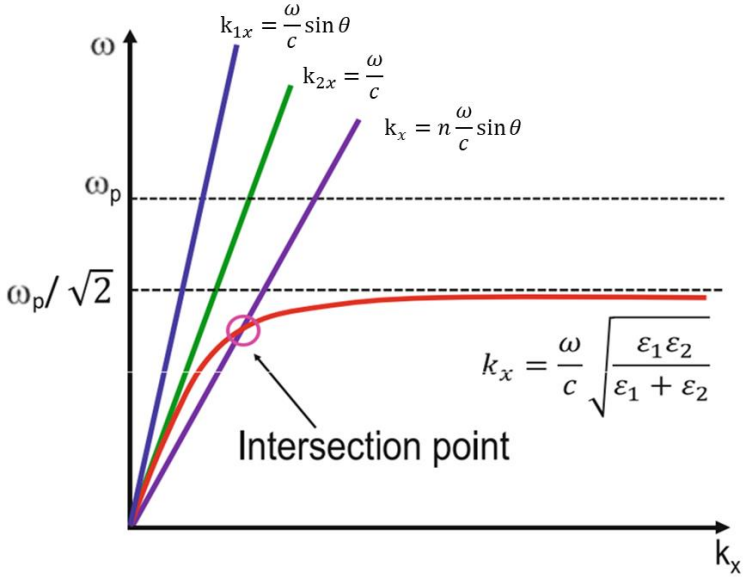

Figure 2. 1 (adopted from Rubio [23]) "Dispersion curves for surface plasmons, light in air ($k_x = \frac{\omega}{c}$), light in air at a certain incident angle ($k_x = \frac{\omega}{c}\sin\theta$), and light in a dielectric medium such as glass at a certain incident angle ($k_x = n\frac{\omega}{c}\sin\theta$)."

2.2.1 Prism Coupling

The main two methods that use prism coupling to excite SPs with the incident light are Kretschmann-Raether and Otto configurations [14], [41]. Both of these methods use the attenuated total reflection (ATR) approach through a prism coupler. In the Kretschmann-Raether configuration, a thin metal film is sandwiched between a high refractive index dielectric prism (such as glass) and air, and the incident wave is from the dielectric side. When an electromagnetic wave propagating in the prism is made incident on the metal film, a part of the

wave is reflected back into the prism, and a part of it penetrates through the metal [42]. This penetrated wave decays exponentially in the direction perpendicular to the prism–metal interface as an evanescent wave. If the metal film is sufficiently thin (less than 100 nm for light in visible and near infrared (IR) part of spectrum), at a certain incidence angle, the evanescent wave penetrates through the metal film and couples with the SPs at the outer boundary of the metal film that creates the resonance condition [43]. Under the resonance conditions, a minimum is observed in the reflected light when the evanescent field of the incident light is coupled to SPs.

In the Otto configuration, an air gap exists between the dielectric and the metal, where the evanescent wave generated by ATR at the prism-air interface excites surface plasmons at the air-metal interface. In this method, the arrangement of the air gap must be within the penetration depth of the evanescent wave, which makes it unsuitable for practical applications [44]. Figure 2.2 shows the difference in the geometry of the Kretschmann-Raether and Otto configurations.

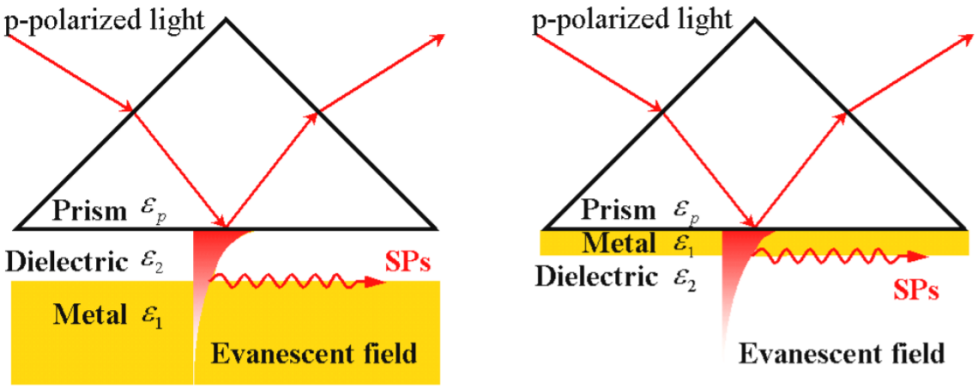

(a) (b)

Figure 2. 2 (Adopted from Sato [45]) "Configurations of the attenuated total reflection (ATR) method: (a) Otto configuration and (b) Kretschmann-Raether configuration."

2.2.2 Grating Coupling

Diffraction effects at a grating pattern on a metal surface can result in the excitation of the SPs. In this approach, as the incident light wave from a dielectric medium reaches to the rough surface of a metal, SPs get excited, and they can propagate at the rough interface between the metal and the dielectric, as shown in figure 2.3. The wavevector of the diffracted light from a rough metal surface can be increased or decreased (based on its incident angle with respect to the normal pf the average plane of the rough surface) and forming a series of diffracted modes. When the incident light wave vector along the interface of a diffracted order is equal to that of SPs, the excitation of SPs can be observed according to the coupling condition [46]:

$$k_{sp} = nk \ \sin\theta \pm mG \tag{12}$$

Where m is an integer number and G = $\frac{2\pi}{\Lambda}$ is the reciprocal vector of the grating, being Λ the grating period.

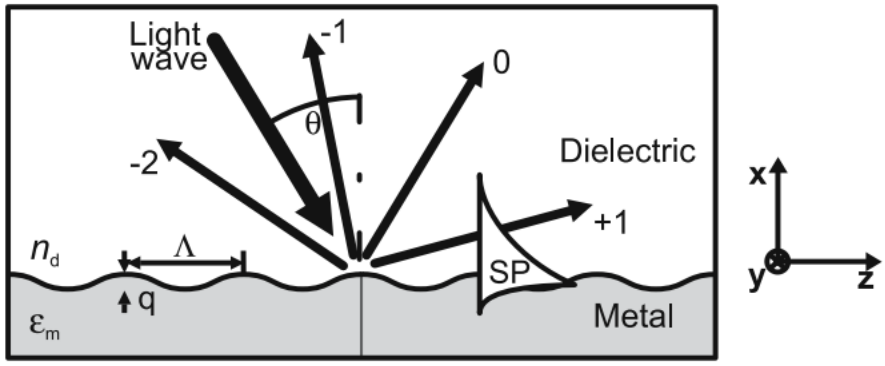

Figure 2. 3 (Adopted from Homola [47]) "Excitation of surface plasmons by the diffraction of light on a diffraction grating."

The main advantage of the grating coupling approach is increasing the wave vector of the incident wave to a high amount, which allows one to excite SPs without using a dielectric

medium (e.g., glass). In other words, grating coupling enables direct excitation possibility and allows us to direct the light beam without utilizing a dielectric medium (whose main role is incrementing the wavevector of the light). However, existing of different diffraction orders and interference of the reflected and diffracted beams increase the complexity of these kinds of systems [48].

2.2.3 Waveguide Coupling

Distributed coupling between a dielectric waveguide and the surface plasmon mode in a metal-coated waveguide is another approach to excite SPs. In this approach, as shown in figure 2.4, a mode of the dielectric waveguide propagates along the waveguide using total internal reflection (TIR), generating an evanescent field at the waveguide/metal interface. This evanescent field penetrates through the metal film and couples with the SPs at the outer boundary of the metal [49], [50].

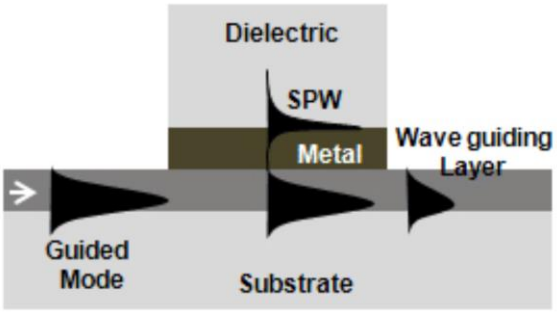

Figure 2. 4 (Adopted from Fan [50]) "Excitation of surface plasmons by a mode of a dielectric waveguide."

When the propagation constant of the created evanescent wave is equal to the real part of the propagation constant of SPs, coupling occurs. Optical fibers are one of the main platforms used

for waveguide coupling, which benefit from the flexibility and low cost [51]. However, the main disadvantage of these structures is the difficulty in the fabrication of uniform and complex nanostructures on top of them.

Chapter 3
Model Setup and Simulation Results

3.1 Device Modelling and Simulation Setup

In this work, to model and simulate a refractive index sensor based on SPR, the wave optics module of COMSOL Multiphysics is used. The model consists of a silica glass layer with a permittivity (ε_S) defined as a function of incident light wavelength (equation 9), and it is designed based on Kretschmann configuration. A thin film of gold is placed on the top of the silica glass layer, followed by the sensing medium with a known refractive index. The values of the experimental refractive indices of gold as a function of the wavelength of the incident light was imposed in the database of the COMSOL to be ensured about the reality of the results [52].

After testing the results of the simulations with different sizes of meshes, the maximum and minimum element sizes were set to 5 nm and 1 nm, respectively. Figure 3.1 shows the effect of the meshing size on the resulting spectra for the device made of a 40 nm thin film. As shown in the figure, reducing the meshing size from the maximum size of 5 nm to 4 nm and minimum size of 1 nm to 0.8 nm, does not change the results significantly, but it increases the simulation time greatly. As a result, the meshing size was fixed on the maximum size of 5 nm and a minimum size of 1 nm.

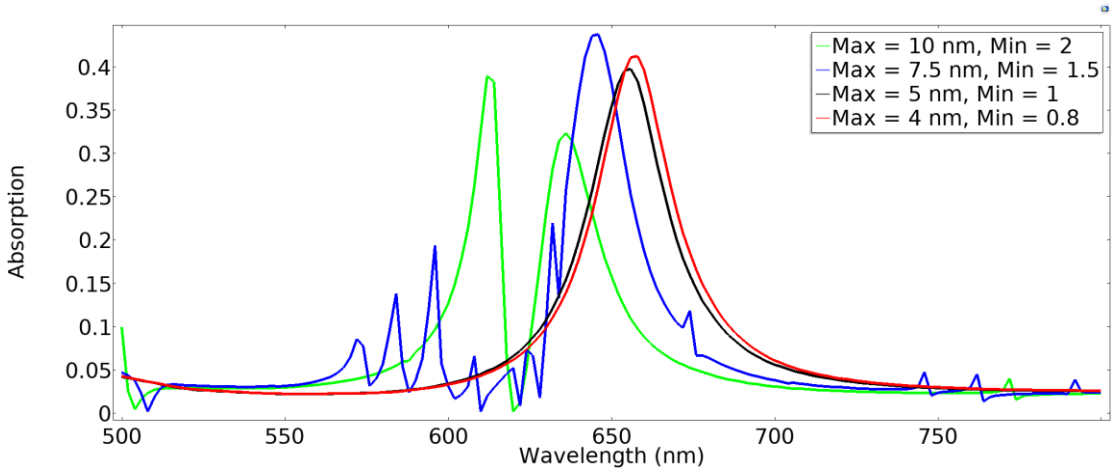

Figure 3. 1 Effect of the meshing size on the resulting spectra of the sensor.

The geometrical configuration of the modeled device is shown in figure 3.2. As it is shown in the figure, Floquet periodic boundary condition (FPBC) was imposed on all plane boundaries along the z-axis of the structure to satisfy the "semi-infinite" condition for the excitation of SPs. This boundary condition assumes that the designed unit cell is repeating periodically in the plane of the gold thin film and creates an infinitely large model (compared to the wavelength of light). On periodic boundaries, the electric field component of the light is defined as [16]

$$E = e^{-jk_F.r} \tag{12}$$

Where r is a vector perpendicular to the symmetry boundaries, and its magnitude is proportional to the distance between the symmetry boundaries, which is automatically defined by the software. The x and y components of the wave vector k_F is defined as

$$k_F = \{k_{Fx}, k_{Fy}\} = \left\{\frac{2\pi}{\lambda}\sqrt{\varepsilon}\,\cos\theta\,, \frac{2\pi}{\lambda}\sqrt{\varepsilon}\,\cos\theta\right\} \tag{13}$$

where θ is the angle between the incident light and the x-y plane, and ε is the permittivity of the periodic mediums.

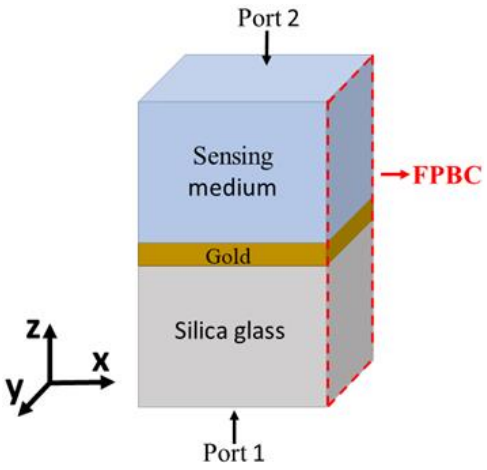

Figure 3. 2 (After Agharazy Dormeny et al. [53]) "3D illustration of the designed unit cell with dimensions of 20 nm× 20 nm× 2 µm. FPBC is imposed on all vertical faces of the cell."

When the wave vector of the incident electromagnetic wave matches the wave vector of the electrons oscillating on the surface of the metallic film, resonance occurs [13]. Hence to excite SPs, it is required to have the components of the electric field acting along the metal-dielectric interface. As a result, the excitation of the SPs can only be done using p-polarized incident light. P-polarized incident light, which refers to as transverse-magnetic wave (H_{TM}) at port 1, is defined as

$$H_{TM} = \left\{0, e^{-j(\frac{2\pi}{\lambda}\sqrt{\varepsilon_S}\cos\theta.x + \frac{2\pi}{\lambda}\sqrt{\varepsilon_S}\sin\theta.z)}, 0\right\} \quad (14)$$

in which the terms ε_S, λ and θ are the same as defined in equations 9 and 13.

3.2 Simulation Results

3.2.1 SPR in Planar Thin Films

To effect of the metallic layer thickness on the device performance was investigated using thin films with thicknesses of 20, 40, 60, and 80 nm in the mentioned design. To check the performance of the sensor, glycerol with a refractive index of 1.357 was considered as the

sensing medium, and the absorption spectrum with wavelengths ranging from 300 to 850 nm was obtained.

Figure 3.3.a shows the absorption spectra of the mentioned devices. The observations demonstrate two distinct regions in the spectrum, inter-band (IB) and SPR. Excitation of the electrons from lower shells of the gold atom to the conduction band by the incident light creates the IB region in near-UV wavelengths. In this region, the position of the peaks is not dependent on the thickness, shape, and configuration of the metallic thin film [54], and they were observable as we used the experimental data of gold refractive index in our model [55]. The difference in the value of incident light frequency and plasma frequency is the main reason for the occurrence of the IB region. When the frequency of the incident light is greater than the plasma frequency (ω_p), SPs radiate out of surface and they are called radiative SPs. Plasma frequency can be obtained from the following relationship:

$$\omega_p = \sqrt{\left(\frac{Ne^2}{\varepsilon_0 m_e}\right)} \tag{15}$$

where N is the concentration of free electrons, ε_0 is the free-space permittivity and e and m_e are the charge and mass of an electron, respectively [56]. The existence of a SP on a metal/dielectric interface is confined to wavelengths longer than a certain critical wavelength, which depends on the plasma frequency and type of metal. For metals such as gold, silver, and aluminum, this critical wavelength lies in the UV or visible region [13].

In the SPR region of figure 3.3.a, increasing the thickness of the gold layer induces a red-shift in the position of the resonance wavelength. Among the devices investigated in this study, the one with a 40 nm gold film showed the highest amount of absorption at the wavelength of 656 nm. Moreover, the device showed the best resolution (smallest FWHM) compared to the

other devices. By increasing the thickness of the gold layer above 40 nm, the FWHM increases, and its peak is lowered significantly.

The sensitivity of the sensor, S_n, is defined as

$$S_n(\frac{nm}{RIU}) = \frac{\delta\lambda_{res}}{\delta n_d} \quad (16)$$

where $\delta\lambda_{res}$ is the amount of the redshift induced by the change in the refractive index of the dielectric medium by δn_d [57].

Two dielectric materials (glycerol with a refractive of 1.357, shown by solid lines in figure 3.3.b, and pure water, shown by dotted lines in figure 3.3.b, with a refractive index of 1.333) were considered to compare the sensitivity of the sensors made of thin films with 20, 40, and 60 nm thickness. The change in the position of the resonance peaks versus the refractive index of the surrounding fluid is also shown in figure 3.3.b. As one can observe, in all the devices, as the refractive index of the surrounding medium is increased, the resonance wavelength has a red-shift. The sensitivity of the device made of the 60 nm thin film is the largest among the studied devices, and it is equal to 1833 $\frac{nm}{RIU}$ compared to 1666 $\frac{nm}{RIU}$ and 833 $\frac{nm}{RIU}$ for the devices modeled with 40 and 20 nm thin films, respectively.

Although the sensitivity of the 60 nm-model was slightly higher than that of 40 nm-device, the latter showed higher accuracy due to its lower FWHM. Therefore, the 40 nm-model was chosen for further studies. The effect of the pattern of the thin film and its configurations on the performance of a SPR-based device are explored in the following sections.

The electric field distribution at the resonance wavelength for the model made of 40 nm gold thin film is shown in figure 3.3.c. The exponential decay in the value of the electric field in both sides of the metal-dielectric interface confirms that the observed absorption is because of the excitation of the SPs. The decay length of 204 nm is observed for this sensor. This value is

defined as the distance, in which the electric field strength reduces to %37 of the peak amplitude at the metal-dielectric interface [58].

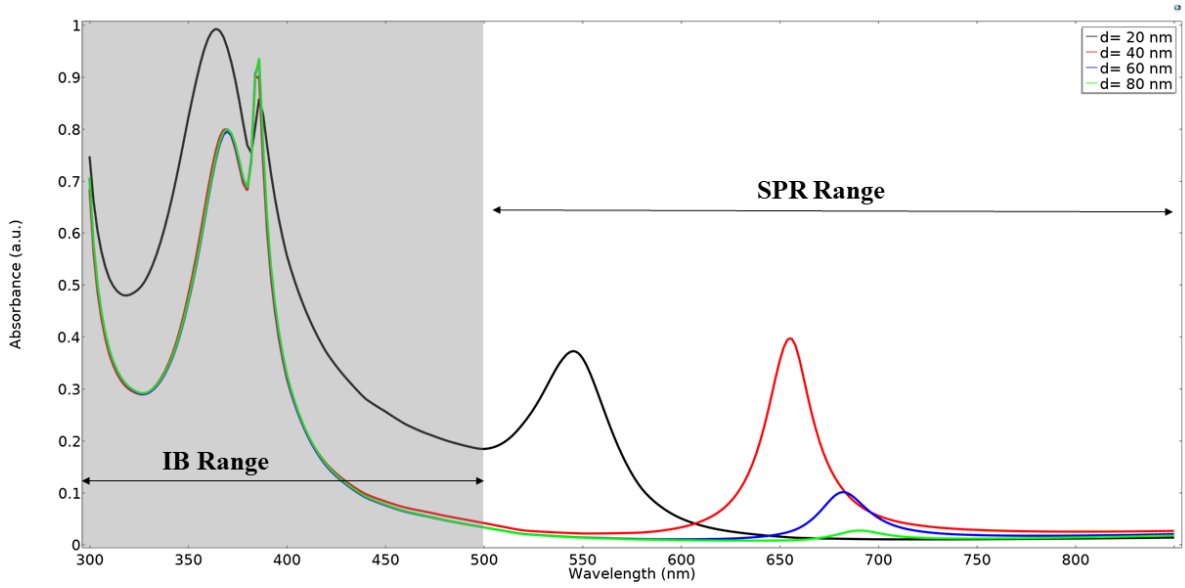

(a)

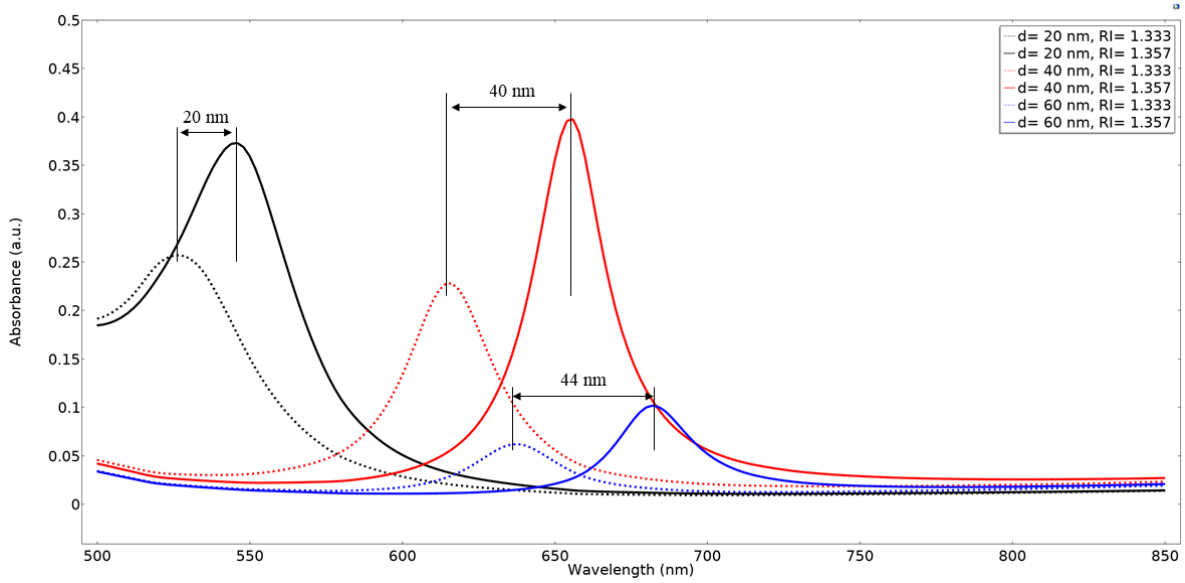

(b)

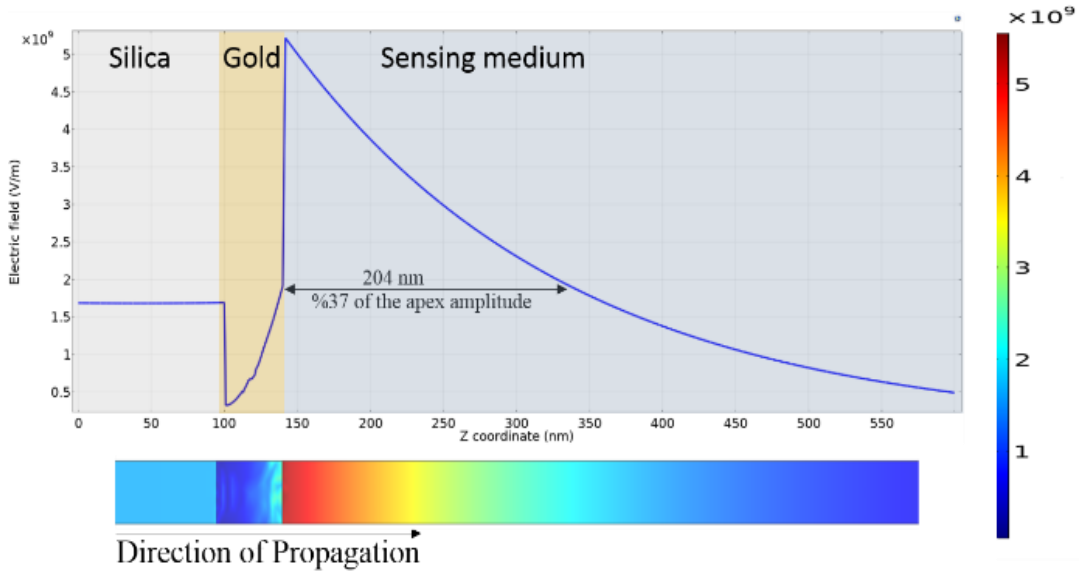

(c)

Figure 3. 3 (After Agharazy Dormeny et al. [53]) "a) The absorbance spectra of the designed devices with gold thin film thicknesses of, 20, 40, 60 and 80 nm for detecting glycerol as the sensing medium (n=1.357), b) The red-shift of the resonance wavelength of the sensors made of 20, 40 and 60 nm thin film of gold as the refractive index of the medium is increased from 1.333 (dotted lines) to 1.357 (solid lines), and c) SPR decay length of 204 nm toward the dielectric region for the 40 nm thin film sensor (color legend shows the distribution of electric field in $\frac{V}{m}$ unit)."

3.2.1.1 Data Validation

In order to explore the verification of the results obtained for the thin films, it is necessary to compare the theoretical results with the experimental ones. Figure 3.4 shows the experimental results obtained by Suzuki et al. for different thicknesses of gold thin films for the detection of distilled water [59].

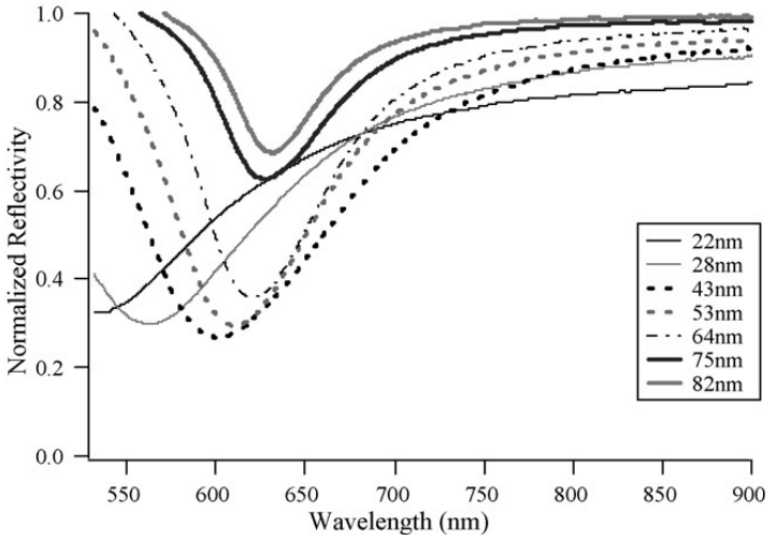

Figure 3. 4 (adopted from [59]) "Collection of typical SPR spectra for the distilled water. The resonance wavelength shifts towards the longer-wavelength region as the gold thickness increases, and the minimum reflectance and the FWHM vary with changing gold thickness."

As shown in the figure, the minimum reflectance (maximum absorption) has occurred in the same range as the simulations results showed. Moreover, increasing the thickness of the thin film has resulted in red-shifting the resonance wavelength, as well as changing the FWHM of the spectra.

Figures 3.5.a and 3.5.b show the experimental data obtained by Iga et al. to detect various samples with refractive indices ranging from 1.333 to 1.398 [60]. In this work, a 5 nm layer of Chromium is coated on the cladding of an optical fiber, and then gold thin films were coated on the Chromium layer. In both figures, the results show that by increasing the refractive index of the sensing medium from 1.333 to 1.357, the amount of absorption is increased, which agrees with the theoretical data obtained using COMSOL in our work. Moreover, structures with 40 nm gold films show higher absorption values compared to the ones with 60 nm thickness, which has consistency with our simulation results.

Regarding comparing the exact values of the absorption peaks, and the position of the peaks, one should note that any small changes in the geometry and structure of the metallic films (such as porosities, surface roughness, existing of other materials, etc.) or small changes in the refractive index of the sensing medium can result in a change in the position and value of the resonance peak. As a result, to investigate the correctness of the simulation data, it would be better to notice the wavelength range in which resonance occurs, and the trend of the results.

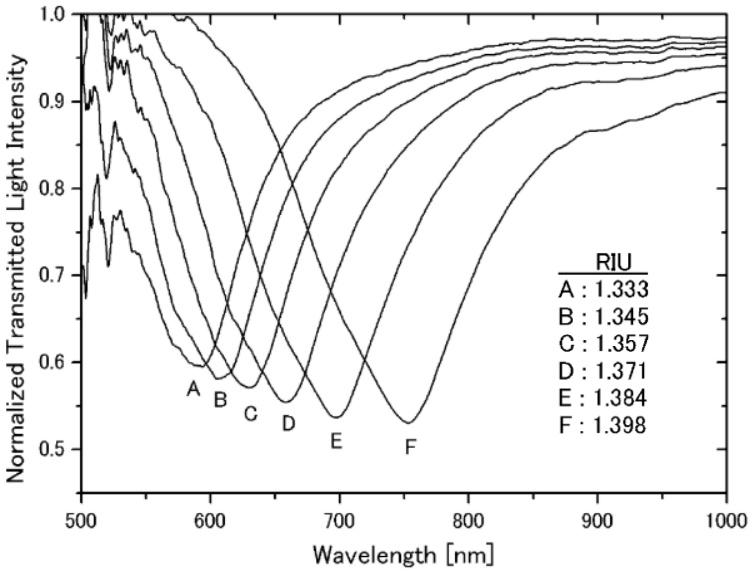

(a)

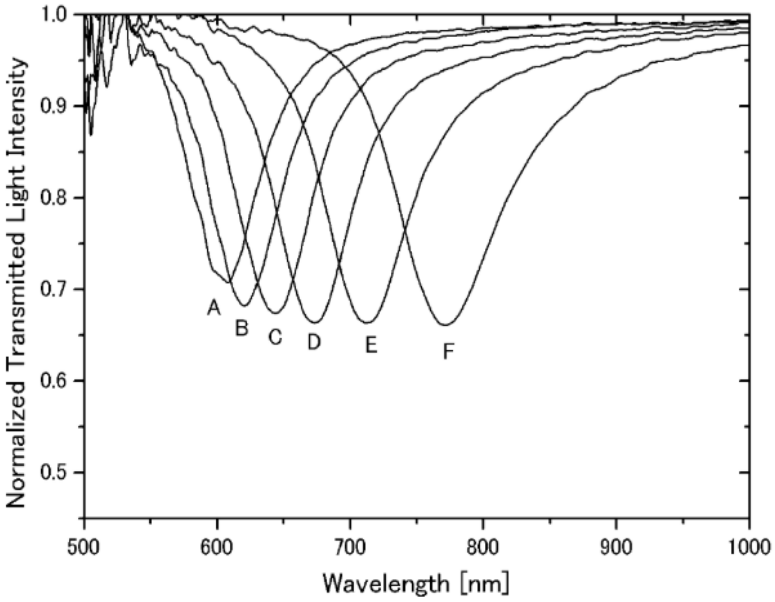

(b)

Figure 3. 5 (adopted from [60]) "Experimentally obtained SPR spectra for two different Au thickness fiber sensors: thickness (nm) = (a) 40 nm, (b) 60 nm."

3.2.2 Nanovoid and Nanohole Patterned Thin Films

In the second step, a thin film of gold with a thickness of 40 nm perforated with arrays of cylindrical cavities is modeled to investigate SPR in thin films patterned with periodic structures. In this model, cavities with a diameter of 10 nm were designed through the thin film, and the effect of the depth of the cavities is investigated for four values of 10, 20, 30, and 40 nm. In this context, "*nanovoid"* is referred to cavities in the metal film, which are supported on a continuous thin film (with a depth of 10, 20 and 30 nm), and "*nanohole*" is referred to the holes with a depth of 40 nm, which are created in a thin film. Two different materials with refractive indices of 1.333 and 1.357 were considered to study the sensing characteristics of the sensors.

Figure 3.6 shows the absorption spectra of the modeled devices. As it is seen, all the perforated thin films result in higher intensity absorption peaks compared to that of the planar

thin film. As the depth of the cavity increases, the absorbance is increased, and it reaches the maximum value for the structure with 30 nm-nanovoids. The sensitivity values of 1750 $\frac{nm}{RIU}$, 1830 $\frac{nm}{RIU}$ and 2083 $\frac{nm}{RIU}$ were obtained for the sensors made of nanovoid with depths of 10, 20, and 30 nm, respectively.

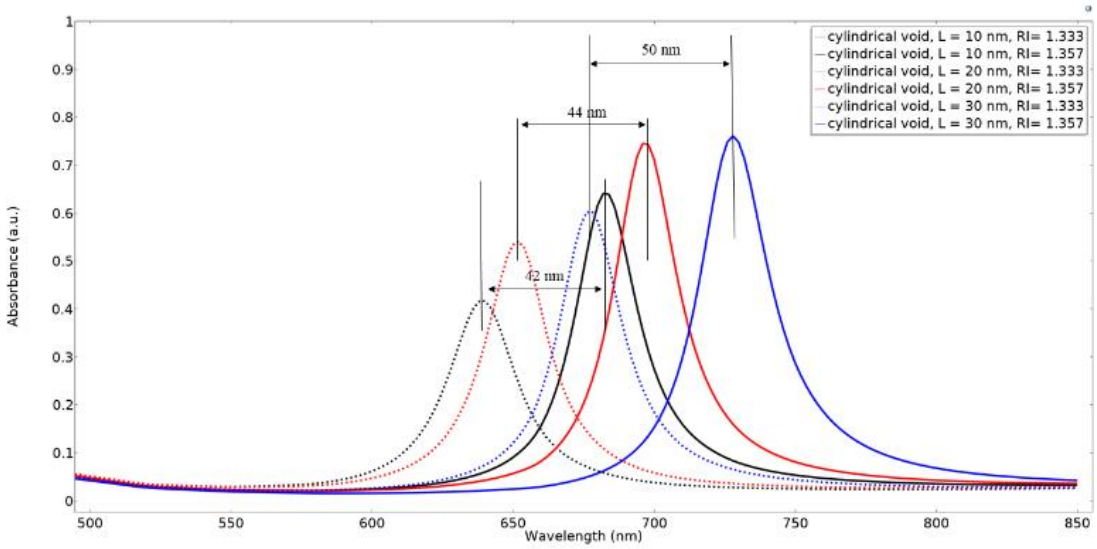

Figure 3. 6 (After Agharazy Dormeny et al. [53]) "The absorption spectra of the devices made from cylindrical nanovoid arrays with various depths of 10, 20 and 30 nm for the refractive indices of 1.333 (dotted lines) and 1.357 (solid lines)."

The same study is performed for the sensor patterned with nanohole arrays, and the effect of the conformation of the hole (cylindrical and cubic) is further investigated. The optical absorption spectra of the devices made of a 40 nm thin film perforated with cubic holes (10 nm× 10 nm× 40 nm) or cylindrical holes (with a diameter of 10 nm) for two refractive indices of 1.333 and 1.357 is shown in figure 3.7. According to this figure, both sensors show approximately the same sensitivities and accuracies. The sensitivity of 1916 $\frac{nm}{RIU}$ for the sensors made of cylindrical nanohole marginally improved to 2000 $\frac{nm}{RIU}$ for sensors with cubic nanoholes.

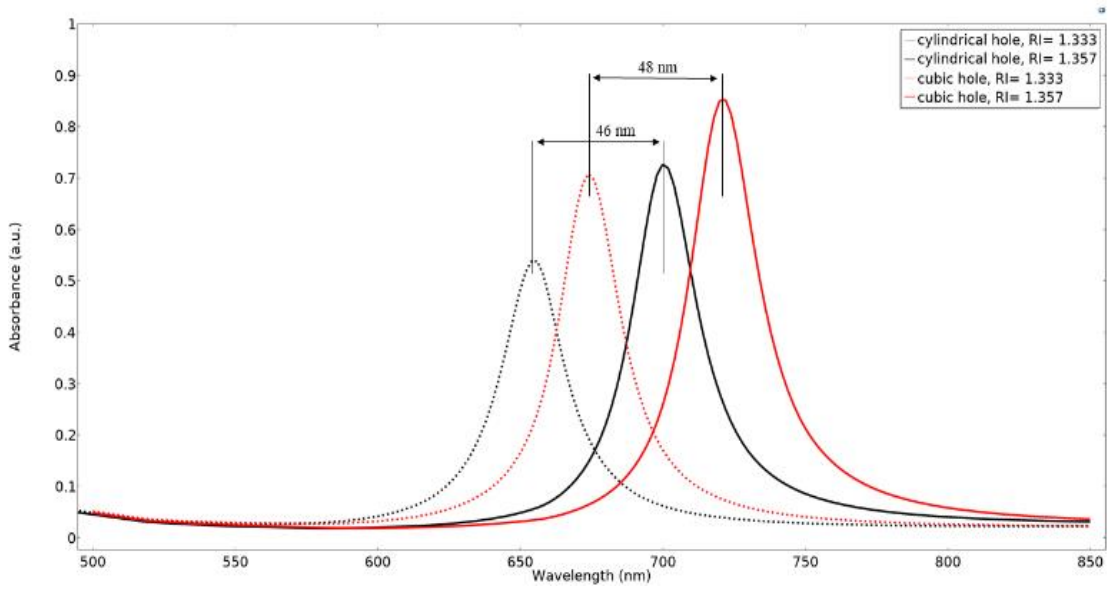

Figure 3. 7 (After Agharazy Dormeny et al. [53]) "The absorption spectra of the devices made from cubic/cylindrical nanohole arrays for two refractive indices of 1.333 (dotted lines) and 1.357 (solid lines)."

Comparing the field enhancements due to the excitation of the SPs at resonance condition can help for further understanding of the physics of these phenomena. In this case, the electric field profiles of the devices, which showed the highest sensitivity, are compared. The electric field distribution of the 30 nm nanovoid-sensor is shown in figure 3.8.a. As one can see, a strong coupling between the evanescent wave and the SPP modes occurs on the upper rim of the nanovoid on the metal-dielectric interface.

Figure 3.8.b shows the variations of the electric field intensity over a cut line defined along the z-axis of the modeled structure. The geometry of the device and the position of the mentioned cut line are shown in the inset of the figure schematically. Considering the electric field distribution shown in figure 3.8.b and comparing it with figure 3.3.c (SPR in a planar thin film), it can be concluded that the device is supporting both SPR and LSPR modes. The first peak in figure 3.8.b with lower intensity and higher decay length refers to SPR mode. The sharp

peak at the metal-dielectric interface with a higher intensity (about one order of magnitude) and a very small decay length refers to the excitation of the LSPR modes in the sensor [61].

As shown in figure 3.8.c, when the design of the nanostructure changes from nanovoid to nanohole, localization occurs at both upper and lower rims of the hole, which results in higher amounts of absorption (figure 3.7) compared to what showed by devices with nanovoid arrays (figure 3.6). The field intensity graph along a cut line in the z-axis through the geometry is shown in figure 3.8.d. The inset illustrates the position of the cut line schematically. Observation of two sharp peaks at both of the gold interfaces indicates the occurrence of LSPR in both lower and upper rims of the structure. By changing the position of the cut line in a way not to cut through the holes (figure 3.8.e), the variation of the electric field shows only the SPR mode of the device. By comparing the graphs shown in figure 3.8.d and figure 3.8.e, one can conclude that the perforated thin films with nanohole arrays can support both SPR and LSPR modes.

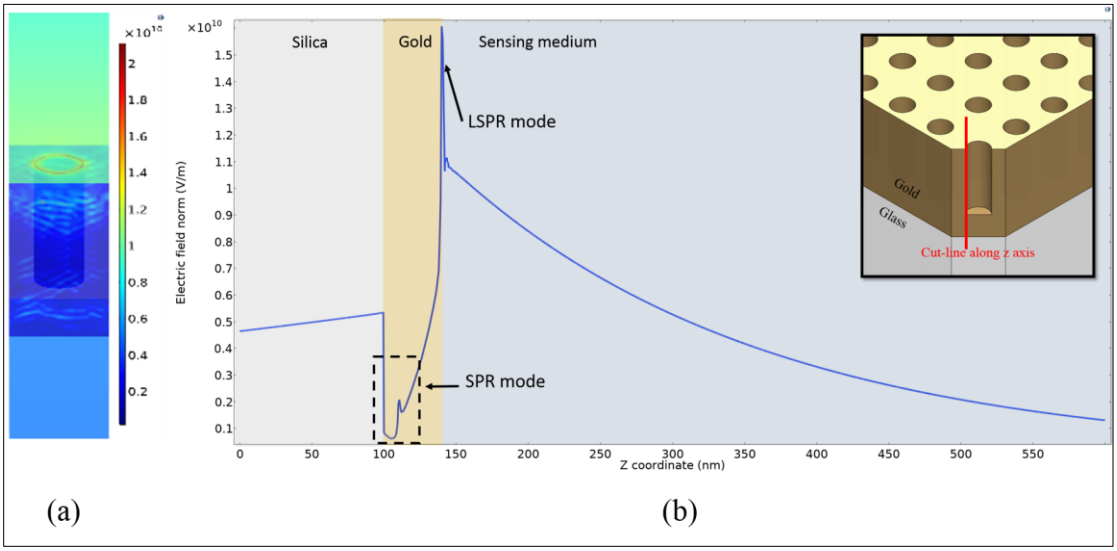

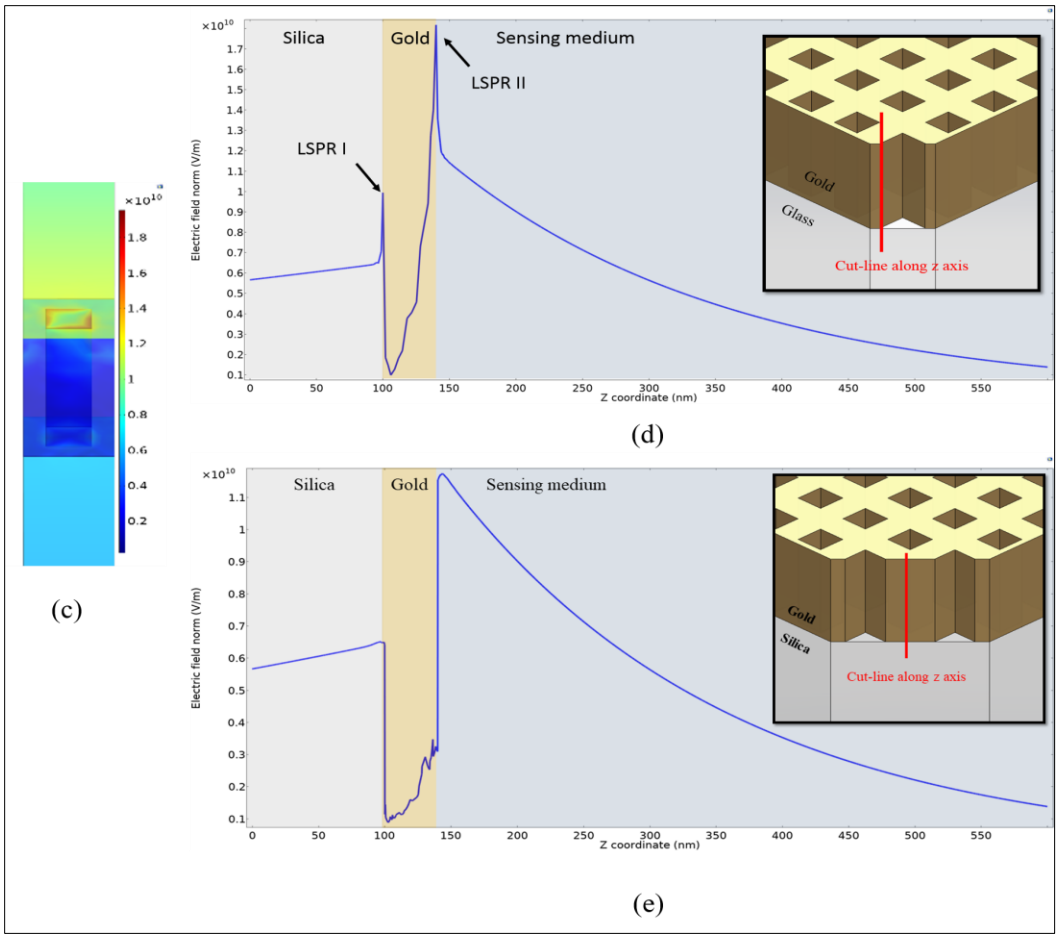

Figure 3.8 (After Agharazy Dormeny et al. [53]) "a-b) The Electric field profile in 30 nm-nanovoid sensor at the resonance wavelength, (a) 3D unit cell (b) along a cut line as shown in the inset. c-e) The Electric field profile in cubic nanohole-device at the resonance wavelength, (c) 3D unit cell, (d) along a cut line which passes through the film discontinuities (as shown in the inset), (e) along a cut line (as shown in the inset) through the thin film. By comparing the graphs shown in (d) and in (e), it can be observed that SPR occurs throughout the continues thin film, while LSPR occurs at film discontinuity boundaries with sharp edges."

3.2.3 Protrusive Thin Films

To study the effect of the protrusive features on the performance of the sensor, two shapes of cubic and cylindrical protrusive features were placed over a 40 nm thin film. In this model, arrays of gold nanowires are implemented above the 40 nm gold thin film. The effect of the

height and shape of the nanowires (cylindrical or cubic conformations) was studied by investigating the performance of the sensors made of 10, 20, 30, and 40 nm gold nanowires. The same method mentioned in sections 3.2.1 and 3.2.2 was used to investigate the refractive index sensitivity of the device for two materials with refractive indices of 1.333 and 1.357.

Figure 3.9 shows the absorption spectra of the devices made of cylindrical nanowires with various lengths. As one can observe, comparing to the results in the previous sections, the resonance wavelengths are shifted toward the IR region. Moreover, as the height of the nanostructure is increased, the resonance wavelength is red-shifted. However, considering the FWHM of the sensors, as the height of nanowires increases, the accuracy of the device is decreased. The same study was performed for the cubic nanowires, and the detailed results of the models based on the absorption spectra of the sensors are presented in table 3.1.

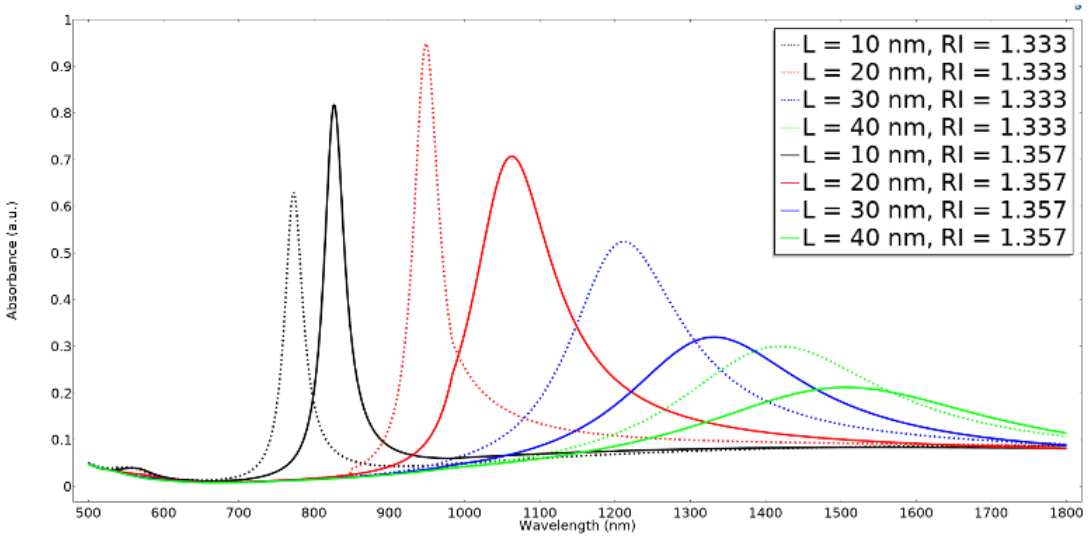

Figure 3. 9 (After Agharazy Dormeny et al. [53]) **"**Absorption spectra of the sensors made of nanowires with various lengths of 10, 20, 30 and 40 nm supported by 40 nm thin film for two materials with refractive indices of 1.333 and 1.357."

Comparing the results obtained from the cylindrical and cubic nanostructures, structures with cylindrical nanowires show higher sensitivity than those with the cubic nanowires at the same height. Furthermore, increasing the height of the nanowires up to 30 nm increases the sensitivity of the sensors. When the height of the nanowire goes above 30 nm, the sensitivity of the device shows a decreasing trend for both cylindrical and cubic geometries. In this study, the highest sensitivity achieved for the sensors made of protrusive thin films was 4916 nm/RIU for the device containing 30 nm cylindrical nanowire supported by the 40 nm thin films.

Considering the obtained results (sensitivity and FOM) for all the designed structures (planar thin film, nanovoid/nanohole array patterned thin film, and protrusive thin film), the device made of 20 nm cylindrical nanowires can be considered as the optimum design for the detection of liquids since both the sensitivity and FOM values are high for this device. FOM is defined as the ratio of sensitivity to the FWHM of the device ($^{S_n}/_{FWHM}$), and it is given as 1/RIU. This parameter considers the capability of a given device to sense a given change in the location of the maximum of absorption. In addition to the cylindrical and cubic nanostructures presented in table 3.1, to investigate the effect of shape of the nanowires (with an equal length), two types of pyramidal structures with aspect ratios of 1 and 0.5 were also considered. The performance parameters of all of the designed structures (with a thin film thickness of 40 nm and nanowire length of 20 nm) are shown in table 3.2, and the electric field distributions at the resonance wavelength are shown in figure 3.10. As can be seen in table 3.2, cylindrical nanowires can be still considered as the optimum structure for the proposed sensor. Consequently, to narrow down our investigations, further studies are performed only on this model, which will be discussed in the next chapter.

Table 3.1 (After Agharazy Dormeny et al. [54]) Detailed results based on the absorption spectra

NW Geometry	NW height (nm)	Sensitivity ($\frac{nm}{RIU}$)	FOM ($\frac{1}{RIU}$)	Absorbance (a.u.)	
				RI = 1.333	RI = 1.357
Cylindrical	10	2416	80.43	0.63	0.817
	20	4750	111.45	0.949	0.708
	30	4916	23.91	0.525	0.319
	40	3583	8.84	0.3	0.212
Cubic	10	2333	78.13	0.662	0.841
	20	3291	85.17	0.941	0.676
	30	4875	24.70	0.495	0.298
	40	3416	8.78	0.275	0.194

Table 3.2 Detailed results based on the absorption spectra

NW Geometry	Sensitivity ($\frac{nm}{RIU}$)	FOM ($\frac{1}{RIU}$)	Absorbance (a.u.)	
			RI = 1.333	RI = 1.357
Cylindrical	4750	111.45	0.949	0.708
Cubic	3291	85.17	0.941	0.676
Full Pyramid	2083	57.44	0.63	0.802
Half Pyramid	4666	107.99	0.915	0.8

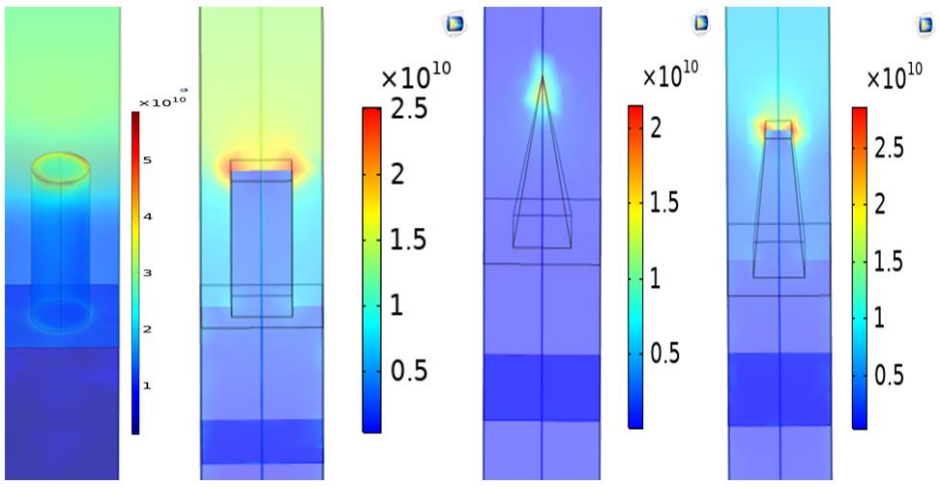

Figure 3. 10 "The electric field intensity for the protrusive thin films with different shapes of nanowires. The length of all the nanowires are 20 nm and the electric field distribution has been taken under resonance condition for the refractive index of 1.333."

3.3 Gas Detection Feasibility

In all the previously mentioned sections, the obtained data are as a result of testing the designed devices to detect liquids (water and glycerol) as the sensing mediums. However, SPR/LSPR-based sensors can also be used to detect various gasses. Similar to other sensing materials, size and configuration of the metallic nanostructure is the main parameter that affects the sensitivity and absorption of the sensors. In this part, the same structures used for liquid sensing are used to explore their capability in detecting gasses.

To check the performance of the device in detecting gasses, the sensing medium has been changed to air (n=1.000293) and Carbon dioxide (n=1.001), and the absorption value and sensitivity of the configurations mentioned in the previous sections have been studied. Figure 3.11 shows the absorption spectra of the devices made by a planar thin film, nanohole patterned thin film, and protrusive thin film (with various lengths of nanowires) for the refractive index of 1.000293. As shown in the figure, no absorption peak was observed for the sensors made of planar thin film and thin films with nanohole patterns. The reason is, since for the detection of liquids the absorption peaks are in the range of 600 nm to 750 nm, the resonance peak has a blue-shift and it does not appear in the range of 350 nm to 1000 nm wavelengths.

On the other hand, for the sensors made of protrusive thin films, since the resonance wavelength in the case of liquid media is in the range of IR, the blue-shift resulted by reducing the refractive index, brings the absorption peak to the visible range. As one can observe in figure 3.11, increasing the height of the nanowires can results in an increase of the resonance wavelength, as well as increasing the amount of absorption.

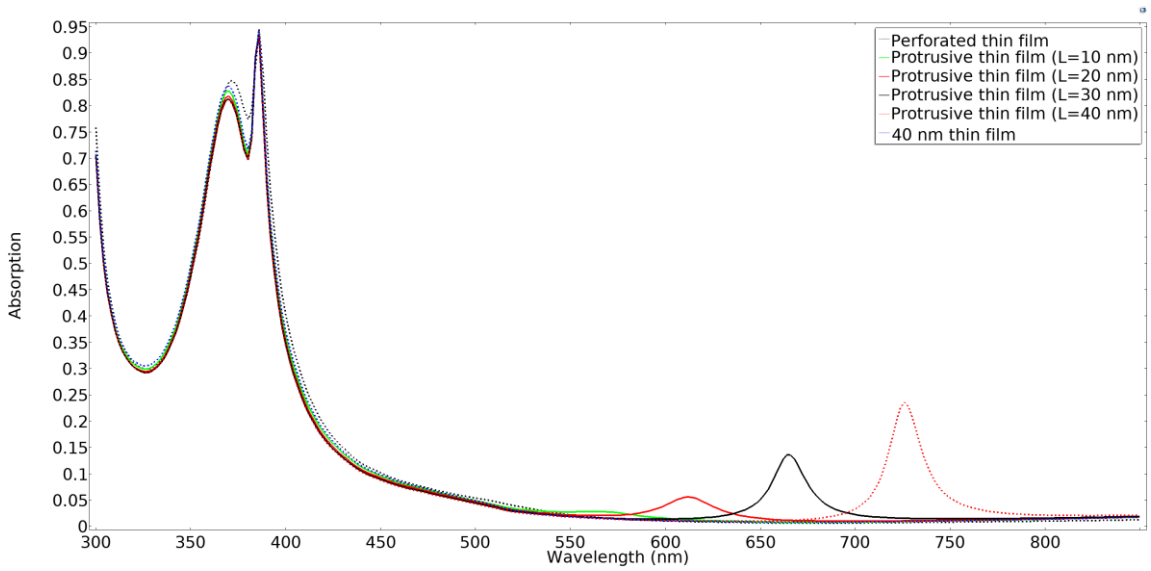

Figure 3. 11 Absorption spectra of the sensors made of planar, perforated, and protrusive thin films for gas detection.

In order to measure the sensitivity of the mentioned devices, two refractive indices of 1.000293 and 1.001 were considered. Due to the small difference in the refractive index values of the mentioned gasses, it was needed to increase the resolution of the simulations by reducing the steps of the sweeps. As shown in table 3.3, increasing the length of the nanowires results in improving the sensitivity of the sensors. In these cases, the sensitivity has risen from 424.3 $\frac{nm}{RIU}$ (for 20 nm nanowire) to 848.6 $\frac{nm}{RIU}$ (for 40 nm nanowire).

Table 3. 3 Detailed results based on the absorption spectra for gas sensing

NW height (nm)	Sensitivity ($\frac{nm}{RIU}$)	Absorbance (a.u.)	
		RI = 1.000293	RI = 1.001
20	424.33	0.0555	0.0558
30	565.77	0.1368	0.1375
40	848.66	0.2356	0.2366

3.4 Conclusion

In this chapter, the simulation steps of the refractive index sensor based on SPR/LSPR were discussed. Three models for the configuration of the metallic thin films (planar thin film, perforated thin film, and protrusive thin film) were considered, and the electric field distribution and absorption spectra of all the devices were investigated.

Initially, it was demonstrated that the thickness of 40 nm for the metallic thin film could result in the best performance (in terms of absorption value, sensitivity, and accuracy) among planar thin films so, the rest of our studies was based on devices made of the 40 nm thin films. It was shown that in devices with perforated thin films, as the length of the nanovoid increases, higher absorptions and larger sensitivities can be achieved. In the case of protrusive thin films, it was observed that they shift the resonance wavelengths to the IR region. Moreover, they provide better performance for the devices compared to those made of planar or perforated thin films. It was concluded that 40 nm protrusive thin films with 10×20 nm (diameter × length) cylindrical nanowires could result with devices with best performance in terms of sensitivity, absorption, and FWHM.

In this work, the physics of SPR and LSPR was studied using the electric field profile of each of the mentioned configurations. As expected, it was observed that in planar thin films, just SPR occurs. However, the electric field profile showed that in nanovoid/nanohole patterned thin films, both SPR and LSPR modes could be excited.

To continue our investigations, the effect of shape of the nanowires on the performance of the SPR/LSPR-based devices was investigated, and it was concluded that cylindrical nanowires could exhibit the best performance among the structures studied in this work.

Finally, the feasibility of using the same nanostructures to detect gasses was discussed. Devices made of planar thin film, nanohole patterned thin film, and protrusive thin film were investigated in this part. It was demonstrated that the devices with planar and perforated thin films do not show any absorption peaks to detect air and carbon dioxide. However, devices made of protrusive thin films showed some shallow peaks and it was observed that as the length of the nanowires increases, the performance of the sensor is improved.

Chapter 4
SPR Study of devices with Protrusive Nanostructures

4.1 Light Propagation in Protrusive Nanostructures

The electric field distribution at resonance wavelength for the sensor made of 40 nm gold thin film with 20 nm cylindrical nanowire is shown in figure 4.1.a. As the figure shows, the electric field is enhanced around the nanowire rims. The plane view of the electric field intensity on a cross-section of the unit cell is shown in figure 4.1.b and 4.1.c. Figure 4.1.b shows the upper rim of the metallic nanowire, and figure 4.1.c demonstrates the lower rim, where the nanowire connects to the thin film. As it is seen, the field enhancement is stronger at the upper rim compared to the lower rim.

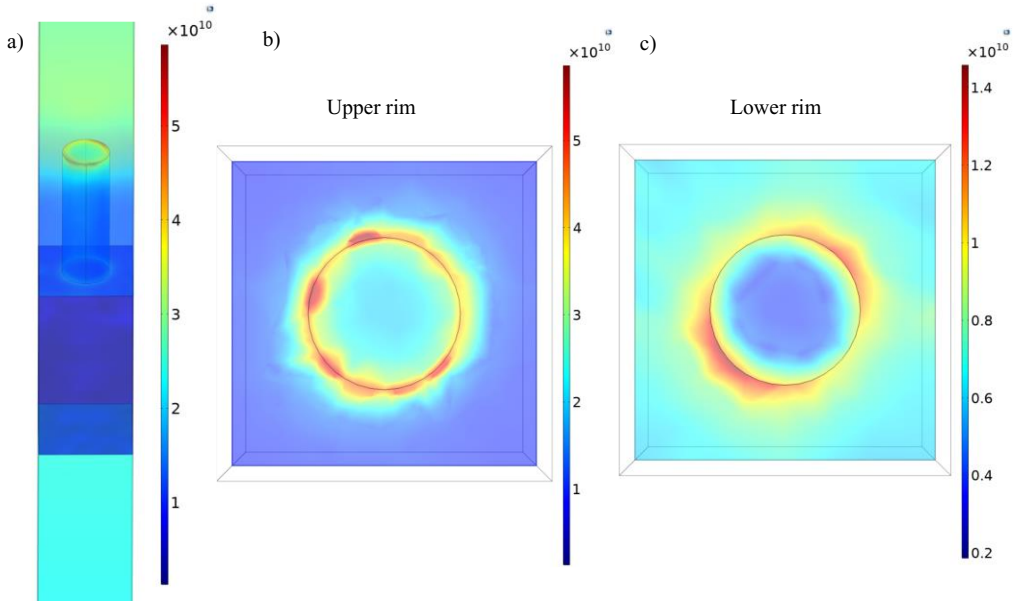

Figure 4. 1 (After Agharazy Dormeny et al. [53]) "Electric field distribution in a 20 nm-nanowire sensor over, a) The unit cell b) Upper rim and c) Lower rim"

Similar to the perforated thin films discussed in the third chapter, the implementation of the metallic nanowire arrays on a metallic thin film can result in the co-excitation of SPR and LSPR modes. The electric field distribution along a cut line through the modeled device structure (the position of the cut line is shown in the inset of the figure) is shown in figure 4.2. As shown in the figure, considering the z-coordination of the structure, the position of the SPR peak is at the lower rim of the nanowire, where it reaches the thin film. By comparing the SPR peak of this device with that of the 40 nm planar thin film shown in figure 3.2.c, it can be concluded that the electric field variation has a similar behavior of the conventional SPR. The sharp peak in figure 4.2 is due to the LSPR mode excitation of the sensor, which can enhance the electric field significantly with a few nm decay lengths.

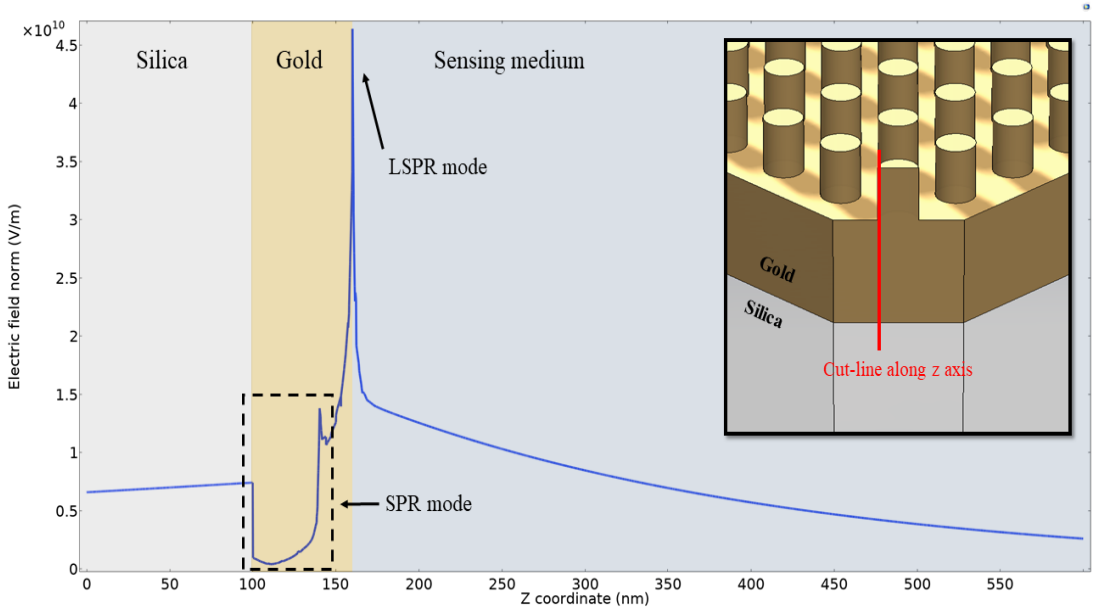

Figure 4. 2 (After Agharazy Dormeny et al. [53]) "The Electric field profile of the sensor made of 20 nm nanowires supported by 40 nm thin film at the resonance wavelength along a cut line as shown in the inset."

The calibration curve of the device made of 20 nm nanowires on a 40 nm thin film is shown in figure 4.3. The graph demonstrates the resonance wavelengths of the sensor for different refractive indices (various sensing materials) and determines the sensing capability of the sensor. Selected substances are purified water, propane, water, ether, glycerol, acetone, acetic acid, and propyl with refractive indices of 1.333, 1.34, 1.346, 1.35, 1.357, 1.36, 1.37 and 1.38, respectively. The linearity in the calibration curve demonstrates that the sensor is capable of identifying the refractive indices of unknown mediums as a function of resonance wavelength. As can be observed in the figure, as the refractive index of the sensing medium increases, the shift in the resonance wavelength is significantly enlarged. This results in higher sensitivity of the sensor for the mediums with higher refractive indices. The slope of the linear fit to the calibration data shows the average sensitivity of the sensor, which is 5847.2 nm/RIU for the studied materials.

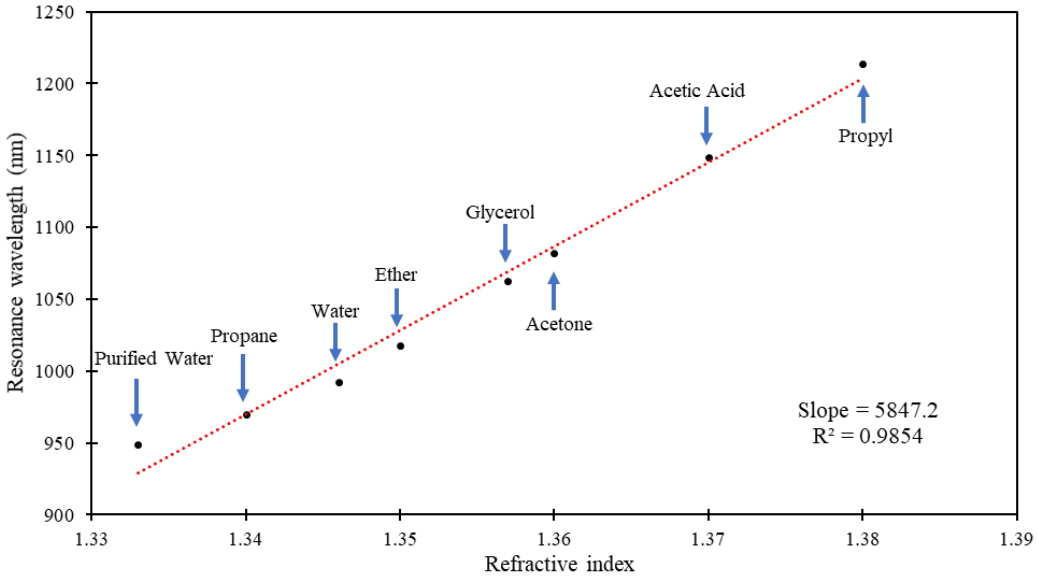

Figure 4. 3 (After Agharazy Dormeny et al. [53]) "The calibration curve of the resonance wavelengths as a function of refractive indices of selected substances. The linear line fitted our

data with R2 of 0.9854. The average sensitivity of 5847.2 is calculated by the slope of the curve."

4.2 Development of the Simulation Software

To reduce the barrier for sharing the simulation platform with people who want to model and simulate their device and see its performance, a COMSOL-based application has been created in the application builder module of COMSOL Multiphysics. In this application, people can change the simulation's parameters such as size of the nanostructures, thickness of the thin film, refractive index of the surrounding medium, etc., and they can observe the result without any prior knowledge of COMSOL. This application provides the opportunity to share the simulation file with people who do not have any information about COMSOL, and they can customize their design for a SPR sensor by just changing the design parameters.

Figure 4.4.a-e shows different windows of the created application. As shown in figure 4.4.a-d, the user can easily define the optical parameters like angle of incidence, refractive index of the sensing medium, and the wavelength range in which they want to sweep the wavelength. Moreover, in the geometry part, the user can change the geometrical factors of the device such as depth and width of the unit cell, thickness of the metallic thin film, and height and diameter of the nanowire. These features allow one to change their design as they want without any knowledge of COMSOL. As shown in figure 4.4.b, by pressing the 'Mesh' button, the application automatically creates the appropriate mesh, and by using the 'Compute' button, it starts to solve the equations and generates the electric field distribution and the absorption spectrum as shown in figures 4.4.c and 4.4.d.

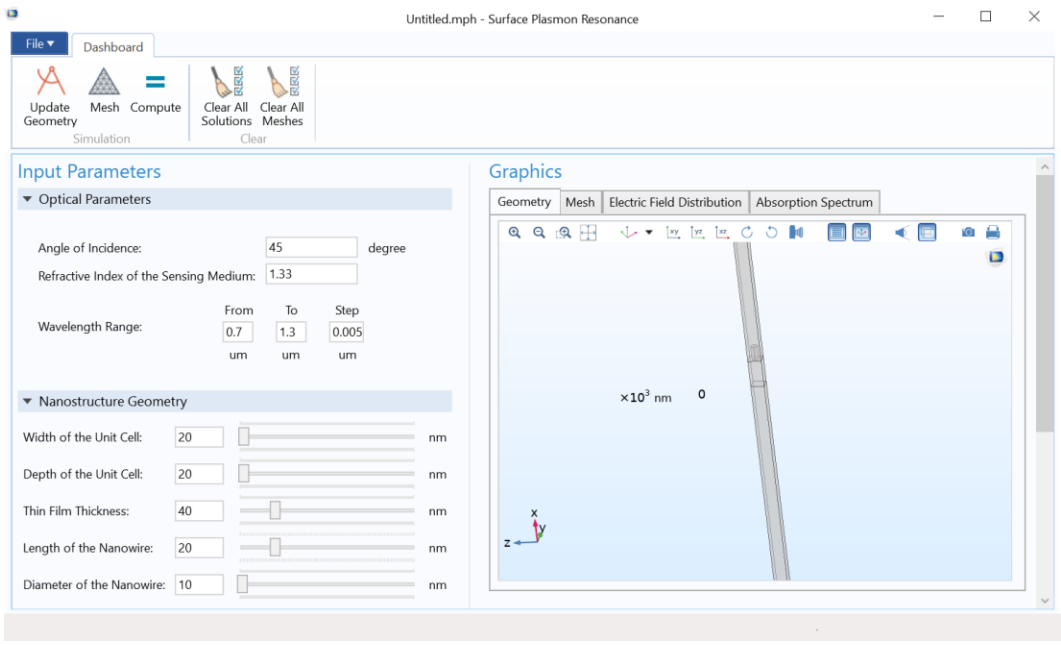
Untitled.mph - Surface Plasmon Resonance
File
Dashboard
Update Geometry
Mesh
Compute
Simulation
Clear All Solutions
Clear All Meshes
Clear
Input Parameters
Optical Parameters
Angle of Incidence:
45
degree
Refractive Index of the Sensing Medium:
1.33
Wavelength Range:
From
To
Step
0.7
1.3
0.005
um
um
um
Nanostructure Geometry
Width of the Unit Cell:
20
nm
Depth of the Unit Cell:
20
nm
Thin Film Thickness:
40
nm
Length of the Nanowire:
20
nm
Diameter of the Nanowire:
10
nm
Graphics
Geometry
Mesh
Electric Field Distribution
Absorption Spectrum
×10³ nm
0
x
y
z

(a)

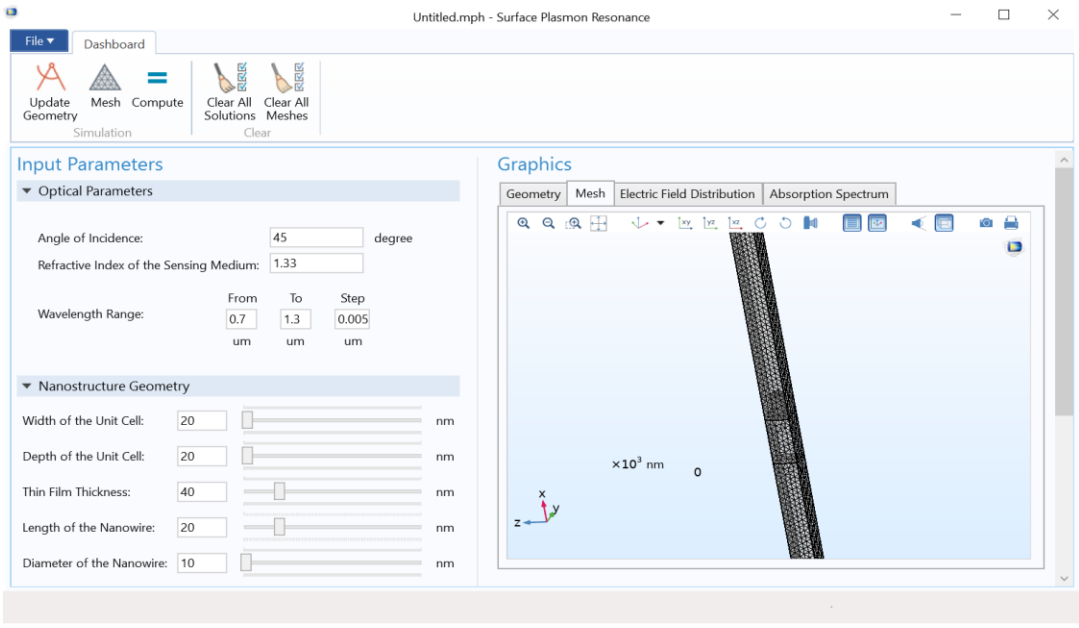
Untitled.mph - Surface Plasmon Resonance
File
Dashboard
Update Geometry
Mesh
Compute
Simulation
Clear All Solutions
Clear All Meshes
Clear
Input Parameters
Optical Parameters
Angle of Incidence:
45
degree
Refractive Index of the Sensing Medium:
1.33
Wavelength Range:
From
To
Step
0.7
1.3
0.005
um
um
um
Nanostructure Geometry
Width of the Unit Cell:
20
nm
Depth of the Unit Cell:
20
nm
Thin Film Thickness:
40
nm
Length of the Nanowire:
20
nm
Diameter of the Nanowire:
10
nm
Graphics
Geometry
Mesh
Electric Field Distribution
Absorption Spectrum
×10³ nm
0
x
y
z

(b)

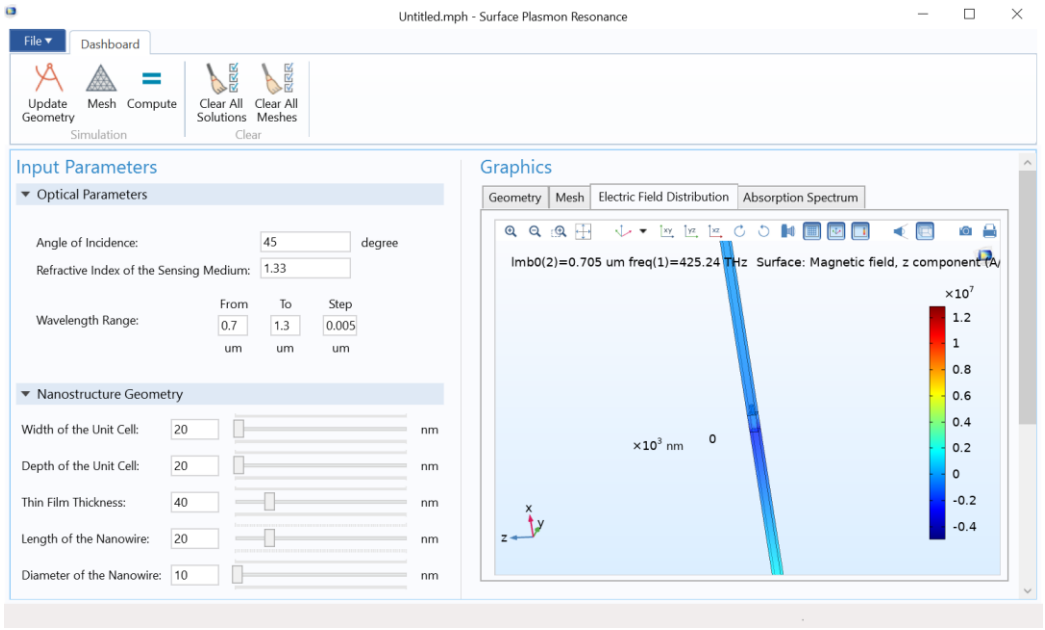
Untitled.mph - Surface Plasmon Resonance
File
Dashboard
Update Geometry
Mesh
Compute
Simulation
Clear All Solutions
Clear All Meshes
Clear
Input Parameters
Optical Parameters
Angle of Incidence: 45 degree
Refractive Index of the Sensing Medium: 1.33
Wavelength Range: From 0.7 um To 1.3 um Step 0.005 um
Nanostructure Geometry
Width of the Unit Cell: 20 nm
Depth of the Unit Cell: 20 nm
Thin Film Thickness: 40 nm
Length of the Nanowire: 20 nm
Diameter of the Nanowire: 10 nm
Graphics
Geometry
Mesh
Electric Field Distribution
Absorption Spectrum
lmb0(2)=0.705 um freq(1)=425.24 THz Surface: Magnetic field, z component (A/
×10^7
1.2
1
0.8
0.6
0.4
0.2
0
-0.2
-0.4
×10^3 nm
0
x
y
z

(c)

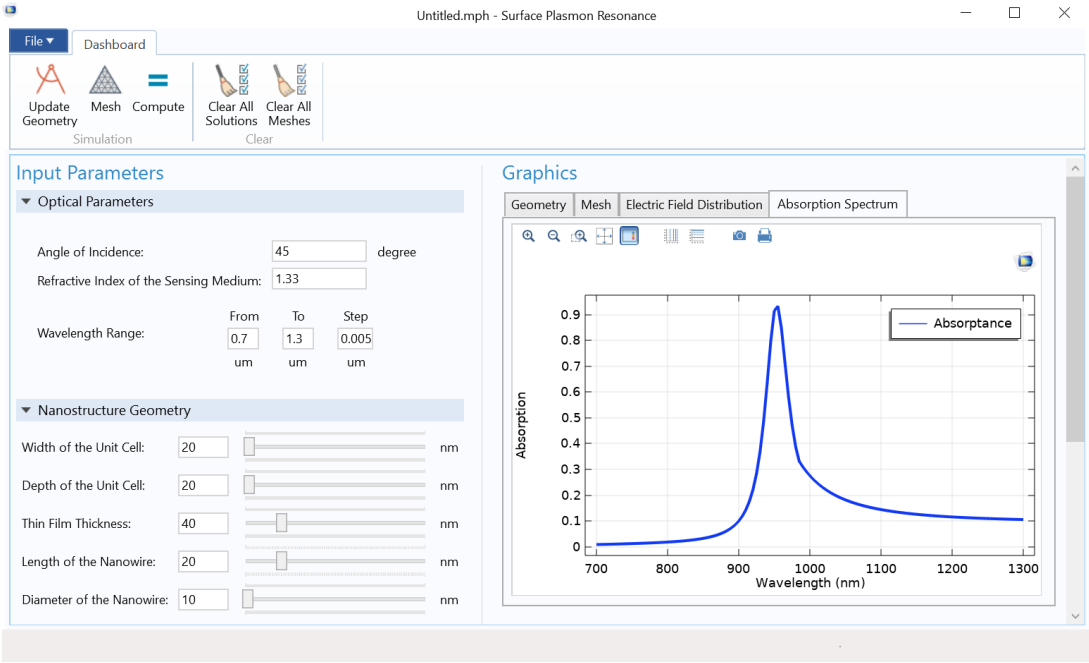
Untitled.mph - Surface Plasmon Resonance
File
Dashboard
Update Geometry
Mesh
Compute
Simulation
Clear All Solutions
Clear All Meshes
Clear
Input Parameters
Optical Parameters
Angle of Incidence: 45 degree
Refractive Index of the Sensing Medium: 1.33
Wavelength Range: From 0.7 um To 1.3 um Step 0.005 um
Nanostructure Geometry
Width of the Unit Cell: 20 nm
Depth of the Unit Cell: 20 nm
Thin Film Thickness: 40 nm
Length of the Nanowire: 20 nm
Diameter of the Nanowire: 10 nm
Graphics
Geometry
Mesh
Electric Field Distribution
Absorption Spectrum
Absorptance
Absorption
0
0.1
0.2
0.3
0.4
0.5
0.6
0.7
0.8
0.9
700
800
900
1000
1100
1200
1300
Wavelength (nm)

(d)

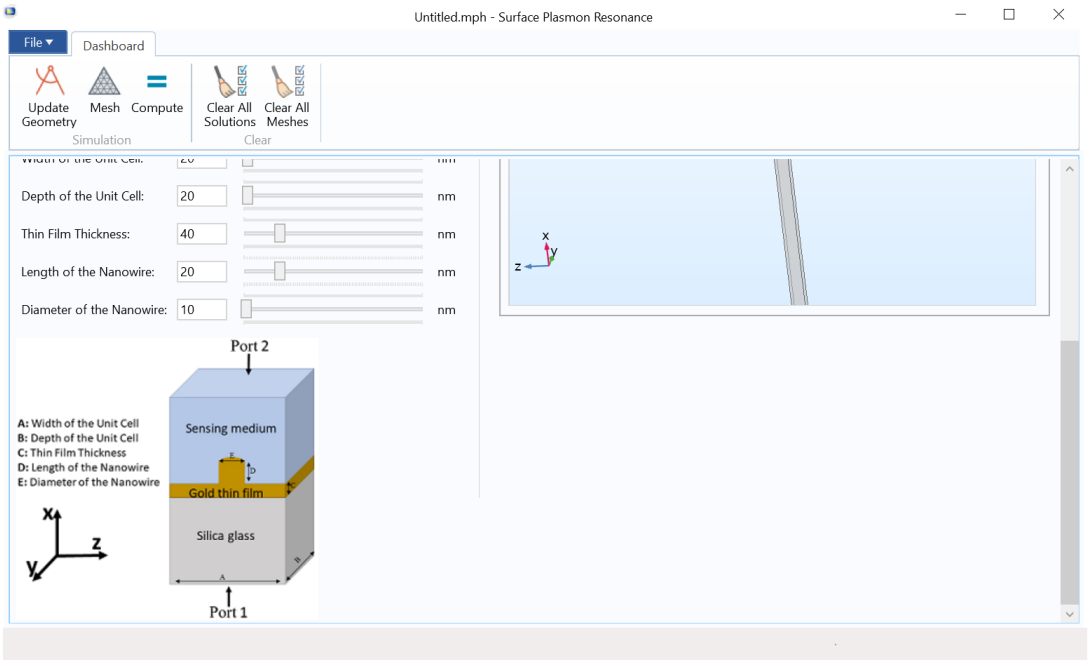

(e)

Figure 4.4 The developed COMSOL-based application to simulate SPR (a) main window and the Geometry tab, (b) Meshing tab, (c) Electric field tab, (d) Absorption graph tab, and (e) the explanation of the simulation parameters.

Chapter 5

Conclusion, Contributions and Future Works

5.1 Conclusion and Contributions

In this work, for the first time, we modeled and simulated a refractive index sensor based on surface plasmon resonance and localized surface plasmon resonance using COMSOL Multiphysics.

To model the device, a silica glass medium was considered and covered with a layer of gold thin film, followed by a dielectric material (used as the sensing medium) at the top of the metallic layer. The performance parameters of the sensor in terms of sensitivity and accuracy were studied as a function of the thin film thickness and its patterned surface. Moreover, the effect of shape of the nanostructures in the case of protrusive thin films on the performance of the device was studied. The investigations showed that patterned metallic thin films could result in the excitation of both SPR and LSPR modes, and consequently, it affects the sensitivity of the device. The absorbance spectroscopy of the investigated models showed that the devices made of 20 nm cylindrical nanowires supported by 40 nm thin film results in the best results in terms of sensitivity and FOM for the detection of liquid substances.

Furthermore, the applicability of the mentioned nanostructures to be used for gas detection was studied. It was observed that planar and perforated thin films do not show any absorption peaks. However, protrusive thin films can be used to detect gasses. It was shown that as the length of the nanowire increases, the performance of the device is improved.

Several substances with various refractive indices were used to measure the resonance wavelength of the device; the variation of resonance wavelength with respect to refractive

indices was plotted. The linear behavior of the plot indicates that the sensor is capable to identify the media with unknown refractive indices.

5.2 Future Works

To improve the obtained results in this research, further investigations can be done to study the effect of the size and periodicity of the patterned structures on the thin film. The investigations can be extended in the following areas:

- As shown in the third chapter, size and configuration of the metallic thin films highly affect the sensitivity, accuracy, and light absorption of the devices. Due to the hardware limitations, in this work, we were not able to increase the size or periodicity of the studied structures. Hence, it is recommended to perform the same studies in the larger dimensions to observe the performance of the SPR-based devices.
- Although the data validation has been performed for the planar thin films and discussed in chapter 3, it is suggested to fabricate the complex nanostructures investigated in this work (perforated and protrusive thin films) and compare the experimental results with the theoretical data.
- In this research, all the simulations were performed using “stationary” conditions in COMSOL. Although “stationary” analysis can help us significantly to investigate the device performance and understand the physics of SPR and LSPR, it is recommended to perform the “time-dependent” analysis as well to study the electric field variations from the very first moment that light reaches to the metallic nanostructures until the time it gets magnified and passes the nanostructures. This study can help for further comprehension of the physics of SPR and LSPR in complex nanostructures.

- One of the interesting features of COMSOL which can be used for future studies is its “Multiphysics” feature which can help to combine the Optics module with other modules (like Chemical Species Transport module) to simulate the reactions of chemicals at the surface of the metallic nanostructures which can result in improving the performance of the sensors.

References

[1] Chen, Jia, Juewen Liu, Xingguo Chen, and Hongdeng Qiu. "Recent progress in nanomaterial-enhanced fluorescence polarization/anisotropy sensors." Chinese Chemical Letters (2019).

[2] Dormeny, A. A., Sohi, P. A., Grudin, D., & Kahrizi, M. (2019). Development of low voltage gas ionization tunneling sensor based on p-type ZnO nanostructures. Sensors and Actuators A: Physical, 299, 111627.

[3] Ullah, N., Mansha, M., Khan, I., & Qurashi, A. (2018). Nanomaterial-based optical chemical sensors for the detection of heavy metals in water: Recent advances and challenges. TrAC Trends in Analytical Chemistry, 100, 155-166.

[4] G. S. KorotÄenkov, *Handbook of Gas Sensor Materials: Properties, Advantages and Shortcomings for Applications. New Trends and Technologies.* 2014.

[5] Yin, M. J., Gu, B., An, Q. F., Yang, C., Guan, Y. L., & Yong, K. T. (2018). Recent development of fiber-optic chemical sensors and biosensors: Mechanisms, materials, micro/nano-fabrications and applications. Coordination Chemistry Reviews, 376, 348-392.

[6] J. Homola, "Surface plasmon resonance sensors for detection of chemical and biological species," *Chem. Rev.,* vol. 108, *(2),* pp. 462-493, 2008.

[7] A. K. Sharma, A. K. Pandey and B. Kaur, "A review of advancements (2007â€“2017) in plasmonics-based optical fiber sensors," *Optical Fiber Technology,* vol. 43, pp. 20-34, 2018.

[8] M. Loos, "Chapter 1 - Nanoscience and Nanotechnology," pp. 1-36, 2015. . DOI: https://doi.org/10.1016/B978-1-4557-3195-4.00001-1.

[9] Anonymous "British Museum Database Image," .

[10] K. Chang, "Tiny is Beautiful: Translating 'Nano' Into Practical," *New York Times 22 Feb 2005: Science,* .

[11] B. D. Gupta and R. Kant, "Recent advances in surface plasmon resonance based fiber optic chemical and biosensors utilizing bulk and nanostructures," *Optics & Laser Technology,* vol. 101, pp. 144-161, 2018.

[12] A. K. Sharma, R. Jha and B. Gupta, "Fiber-optic sensors based on surface plasmon resonance: a comprehensive review," *IEEE Sensors Journal,* vol. 7, *(8),* pp. 1118-1129, 2007.

[13] D. Michel, F. Xiao and K. Alameh, "A compact, flexible fiber-optic Surface Plasmon Resonance sensor with changeable sensor chips," *Sensors Actuators B: Chem.,* vol. 246, pp. 258-261, 2017.

[14] E. Kretschmann and H. Raether, "Radiative decay of non radiative surface plasmons excited by light," *Zeitschrift fÃ¼r Naturforschung A,* vol. 23, *(12),* pp. 2135-2136, 1968.

[15] Mishra, S. K., Tripathi, S. N., Choudhary, V., & Gupta, B. D. (2014). SPR based fibre optic ammonia gas sensor utilizing nanocomposite film of PMMA/reduced graphene oxide prepared by in situ polymerization. Sensors and Actuators B: Chemical, 199, 190-200.

[16] H. Raether, "Surface plasmons on smooth surfaces," in *Surface Plasmons on Smooth and Rough Surfaces and on Gratings*Anonymous 1988, .

[17] Z. Han and S. I. Bozhevolnyi, "Radiation guiding with surface plasmon polaritons," *Reports on Progress in Physics,* vol. 76, *(1),* pp. 016402, 2012.

[18] S. Nivedha, P. R. Babu and K. Senthilnathan, "Surface plasmon resonance: physics and technology." *Current Science (00113891),* vol. 115, *(1),* 2018.

[19] S. O. Kasap, *Optoelectronics and Photonics: Principles and Practices. 340*.

[20] U. Kreibig and M. Vollmer, "Theoretical considerations," in *Optical Properties of Metal Clusters*Anonymous 1995, .

[21] Amendola, V., Pilot, R., Frasconi, M., Maragò, O. M., & Iatì, M. A. (2017). Surface plasmon resonance in gold nanoparticles: a review. Journal of Physics: Condensed Matter, 29(20), 203002.

[22] S. Szunerits, J. Spadavecchia and R. Boukherroub, "Surface plasmon resonance: signal amplification using colloidal gold nanoparticles for enhanced sensitivity," *Reviews in Analytical Chemistry,* vol. 33, *(3),* pp. 153-164, 2014.

[23] A. S. Rubio, *Modified Au-Based Nanomaterials Studied by Surface Plasmon Resonance Spectroscopy.* 2015.

[24] M. A. GarcÃa, "Surface plasmons in metallic nanoparticles: fundamentals and applications," *J. Phys. D,* vol. 44, *(28),* pp. 283001, 2011.

[25] C. Noguez, "Surface plasmons on metal nanoparticles: the influence of shape and physical environment," *The Journal of Physical Chemistry C,* vol. 111, *(10),* pp. 3806-3819, 2007.

[26] C. F. Bohren and D. R. Huffman, "Absorption and Scattering of," *Light by Small,* 1983.

[27] Stuart, D. A., Haes, A. J., Yonzon, C. R., Hicks, E. M., & Van Duyne, R. P. (2005, February). Biological applications of localised surface plasmonic phenomenae. In IEE Proceedings-Nanobiotechnology (Vol. 152, No. 1, pp. 13-32). IET Digital Library.

[28] S. A. Maier, *Plasmonics: Fundamentals and Applications.* 2007.

[29] Pang, L., Hwang, G. M., Slutsky, B., & Fainman, Y. (2007). Spectral sensitivity of two-dimensional nanohole array surface plasmon polariton resonance sensor. Applied Physics Letters, 91(12), 123112.

[30] I. Dolev, I. Epstein and A. Arie, "Surface-plasmon holographic beam shaping," *Phys. Rev. Lett.,* vol. 109, *(20),* pp. 203903, 2012.

[31] M. Couture, S. S. Zhao and J. Masson, "Modern surface plasmon resonance for bioanalytics and biophysics," *Physical Chemistry Chemical Physics,* vol. 15, *(27),* pp. 11190-11216, 2013.

[32] R. B. Sadeghian, *A Field Effect Gas Sensor Based on Self-Standing Nanowire Arrays,* 2007.

[33] P. Abedini Sohi, *Self-Standing Silicon Nanostructures Fabricated using Chemical/Electrochemical Technique: Application in Gas Field Ionization Tunneling Sensor,* 2019.

[34] S. Zuccon, "Plasmonics and near field optics for sensing purposes," 2010.

[35] Huang, Y., Zhong, S., Shi, T., Shen, Y. C., & Cui, D. (2019). HR-Si prism coupled tightly confined spoof surface plasmon polaritons mode for terahertz sensing. Optics Express, 27(23), 34067-34078.

[36] A. Paliwal, M. Tomar and V. Gupta, "Refractive index sensor using long-range surface plasmon resonance with prism coupler," *Plasmonics,* vol. 14, *(2),* pp. 375-381, 2019.

[37] Saito, Y., Yamamoto, Y., Kan, T., Tsukagoshi, T., Noda, K., & Shimoyama, I. (2019). Electrical detection SPR sensor with grating coupled backside illumination. Optics express, 27(13), 17763-17770.

[38] R. Mahmood, M. Johnson and A. C. Hillier, "Massive Enhancement of Optical Transmission across a Thin Metal Film via Wave Vector Matching in Grating-Coupled Surface Plasmon Resonance," *Anal. Chem.,* 2019.

[39] E. Babaei, Z. Sharifi and R. Gordon, "Improving sensitivity of existing surface plasmon resonance systems with grating-coupled short-range surface plasmons," *Josa B,* vol. 36, *(8),* pp. F144-F148, 2019.

[40] Zhang, H., Geng, Y., Xu, S., Xu, W., Tian, Y., Yu, J., ... & Liu, Y. (2019). Surface Plasmon Field-Enhanced Raman Scattering based on Evanescent Field Excitation of Waveguide-Coupled Surface Plasmon Resonance Configuration. The Journal of Physical Chemistry C.

[41] A. Otto, "Excitation of nonradiative surface plasma waves in silver by the method of frustrated total reflection," *Zeitschrift fÃ¼r Physik A Hadrons and Nuclei,* vol. 216, *(4),* pp. 398-410, 1968.

[42] M. Born and E. Wolf, *Principles of Optics: Electromagnetic Theory of Propagation, Interference and Diffraction of Light.* 2013.

[43] R. B. Schasfoort, *Handbook of Surface Plasmon Resonance.* 2017.

[44] B. Gupta, A. Shrivastav and S. Usha, "Surface plasmon resonance-based fiber optic sensors utilizing molecular imprinting," *Sensors,* vol. 16, *(9),* pp. 1381, 2016.

[45] A. Sato, "Surface Plasmon Fluorescence Spectroscopy and Optical Waveguide Fluorescence Spectroscopy in Limit of Detection Studies," *Max Planck Institute for Polymer Research, Johannes Gutenberg University of Mainz, Mainz.Master Thesis,* 2006.

[46] A. P. Hibbins, "Grating coupling of surface plasmon polaritons at visible and microwave frequencies," 2000.

[47] J. Homola and M. Piliarik, "Surface plasmon resonance (SPR) sensors," in *Surface Plasmon Resonance Based Sensors*Anonymous 2006, .

[48] Piliarik, M., Vala, M., Tichý, I., & Homola, J. (2009). Compact and low-cost biosensor based on novel approach to spectroscopy of surface plasmons. Biosensors and Bioelectronics, 24(12), 3430-3435.

[49] R. Harris and J. S. Wilkinson, "Waveguide surface plasmon resonance sensors," *Sensors Actuators B: Chem.,* vol. 29, *(1-3),* pp. 261-267, 1995.

[50] Fan, X., White, I. M., Shopova, S. I., Zhu, H., Suter, J. D., & Sun, Y. (2008). Sensitive optical biosensors for unlabeled targets: A review. analytica chimica acta, 620(1-2), 8-26.

[51] A. Urrutia, J. Goicoechea and F. J. Arregui, "Optical fiber sensors based on nanoparticle-embedded coatings," *Journal of Sensors,* vol. 2015, 2015.

[52] Yakubovsky, D. I., Arsenin, A. V., Stebunov, Y. V., Fedyanin, D. Y., & Volkov, V. S. (2017). Optical constants and structural properties of thin gold films. Optics express, 25(21), 25574-25587.

[53] A. A. Dormeny, P. A. Sohi and M. Kahrizi, "Design and simulation of a refractive index sensor based on SPR and LSPR using gold nanostructures," *Results in Physics,* vol. 16, pp. 102869, 2020.

[54] L. Novotny and B. Hecht, *Principles of Nano-Optics.* 2012.

[55] Yim, Soonmin, Suwan Jeon, Jong Min Kim, Kwang Min Baek, Gun Ho Lee, Hyowook Kim, Jonghwa Shin, and Yeon Sik Jung. "Transferrable plasmonic au thin film containing sub-20 nm nanohole array constructed via high-resolution polymer self-assembly and nanotransfer printing." ACS applied materials & interfaces 10, no. 3 (2018): 2216-2223.

[56] J. Homola, S. S. Yee and G. Gauglitz, "Surface plasmon resonance sensors," *Sensors Actuators B: Chem.,* vol. 54, *(1-2),* pp. 3-15, 1999.

[57] A. K. Sharma and B. Gupta, "On the performance of different bimetallic combinations in surface plasmon resonance based fiber optic sensors," *J. Appl. Phys.,* vol. 101, *(9),* pp. 093111, 2007.

[58] Kaminska, Izabela, Thomas Maurer, Rana Nicolas, Mickaël Renault, Thomas Lerond, Rafael Salas-Montiel, Ziad Herro et al. "Near-field and far-field sensitivities of LSPR sensors." The Journal of Physical Chemistry C 119, no. 17 (2015): 9470-9476.

[59] Suzuki, H., Sugimoto, M., Matsui, Y., & Kondoh, J. (2008). Effects of gold film thickness on spectrum profile and sensitivity of a multimode-optical-fiber SPR sensor. Sensors and Actuators B: Chemical, 132(1), 26-33.

[60] M. Iga, A. Seki and K. Watanabe, "Gold thickness dependence of SPR-based hetero-core structured optical fiber sensor," *Sensors Actuators B: Chem.,* vol. 106, *(1),* pp. 363-368, 2005.

[61] T. Read, R. V. Olkhov and A. M. Shaw, "Measurement of the localised plasmon penetration depth for gold nanoparticles using a non-invasive bio-stacking method," *Physical Chemistry Chemical Physics,* vol. 15, *(16),* pp. 6122-6127, 2013.

[62] Lee, Wei Cheat, Yuanxing Fang, John FC Turner, Jasbir S. Bedi, Christopher C. Perry, Heyong He, Rong Qian, and Qiao Chen. "An enhanced gas ionization sensor from Y-doped vertically aligned conductive ZnO nanorods." Sensors and Actuators B: Chemical 237 (2016): 724-732.

[63] G. Korotcenkov, "Handbook of gas sensor materials," in *Conventional Approaches*Anonymous 2013, .

[64] P. A. Sohi and M. Kahrizi, "Low-voltage gas field ionization tunneling sensor using silicon nanostructures," *IEEE Sensors Journal,* vol. 18, *(15),* pp. 6092-6096, 2018.

[65] R. B. Sadeghian and M. Kahrizi, "A novel miniature gas ionization sensor based on freestanding gold nanowires," *Sensors and Actuators A: Physical,* vol. 137, *(2),* pp. 248-255, 2007.

[66] R. B. Sadeghian and M. Kahrizi, "A novel gas sensor based on tunneling-field-ionization on whisker-covered gold nanowires," *IEEE Sensors Journal,* vol. 8, *(2),* pp. 161-169, 2008.

[67] S. Spitsina and M. Kahrizi, "Application of single-crystalline N-type and P-type ZnO nanowires in miniaturized gas ionization sensor," *Sensors and Materials,* vol. 28, *(1),* pp. 43-54, 2016.

[68] S. Spitsina and M. Kahrizi, "ZnO crystalline nanowires array for application in gas ionization sensor," in *IECON 2012-38th Annual Conference on IEEE Industrial Electronics Society,* 2012, .

[69] R. G. Forbes, C. Edgcombe and U. Valdre, "Some comments on models for field enhancement," *Ultramicroscopy,* vol. 95, pp. 57-65, 2003.

[70] N. Chivu and M. Kahrizi, "Modeling and simulation of a miniaturized gas ionization sensor: Detection of greenhouse gases," *Sensors & Transducers,* vol. 153, *(6),* pp. 105, 2013.

[71] Wahab, R., Ansari, S. G., Kim, Y. S., Seo, H. K., Kim, G. S., Khang, G., & Shin, H. S. (2007). Low temperature solution synthesis and characterization of ZnO nano-flowers. Materials Research Bulletin, 42(9), 1640-1648.

[72] Shao, S., Jia, P., Liu, S., & Bai, W. (2008). Stable field emission from rose-like zinc oxide nanostructures synthesized through a hydrothermal route. Materials Letters, 62(8-9), 1200-1203.

[73] Givargizov, E. I., Zhirnov, V. V., Stepanova, A. N., Rakova, E. V., Kiselev, A. N., & Plekhanov, P. S. (1995). Microstructure and field emission of diamond particles on silicon tips. Applied surface science, 87, 24-30.

Appendix I

Development of low voltage gas ionization tunneling sensor based on p-type ZnO nanostructures

6.1 Introduction

As explained in chapter 2, the principle of operation of physical sensors is based on a physical reaction between the sensing medium and device, such as electron tunneling, light absorption, etc. Gas ionization sensors (GIS) are one of the physical sensors which work based on the fingerprinting of the ionization characteristics of the gasses. These sensors are made up of two conductive parallel plates, which are oppositely charged. When a voltage is applied between the plates, the breakdowns of gasses occur. These breakdowns are usually in the range of a few thousand volts, and the breakdown voltage depends on the type of the gas. By advancing the nanoscience, nanomaterials found their way in GIS. It was found that the required voltage for the sensor (breakdown voltages of gasses) can be significantly reduced by implementing grown nanowires between the two parallel electrodes. Based on the ionization energy and the discharge current of the target gas, GIS can identify a wide range of gasses and they can be calibrated based on either breakdown voltages (gas ionization breakdown sensors, GIBS) or tunneling currents (gas field ionization tunneling sensors, GFITS) [62]-[64].

In this chapter, the development of a GFITS based on p-type semiconductor zinc oxide (ZnO) nanowires is reported. Due to the applied voltages across the parallel electrodes, gas atoms get polarized near the positively biased nanowires' tips, and gas atoms' electrons tunnel

into the nanowires by the field gradient. Among semiconductor materials, the physical properties of ZnO have been at the center of researches for many fields. This semiconductor has a direct wide bandgap of 3.37 eV, and is non-toxic, chemically stable, and biocompatible. Recently, ZnO nanowires have been widely explored to be used in sensing applications, including gas sensors.

The distortion of the atomic potential towards the high electric field gradient for an atom in the vicinity of a p-type semiconductor is schematically shown in figure 6.1. The field effect of the localized electric field at the tip of the nanostructures results in the upward band bending of the atomic potential. In this case, due to the direction of the electric field from the anode to the cathode, holes get accumulated at the surface of the anode, and the surface becomes degenerately p-type. The tunneling of the electrons can only occur in the unoccupied states of the host. As a result, using degenerate p-type semiconductors, which have a large number of available empty energy states in the valence band above the Fermi level, can increase the tunneling probability significantly. Moreover, as stated earlier, the magnitude of the electric field and tunneling probability have a direct relationship. Hence, using high aspect ratio nanowires can amplify the electric field significantly and results in the increasing of the tunneling probability [65]. In order to have electron tunneling, the gas particle must be at a critical distance from the electrode surface. The critical distance is defined as [66]:

$$\boldsymbol{d} = (\boldsymbol{U_I} - (\emptyset + \emptyset_{\boldsymbol{s}}))/\boldsymbol{E} \tag{17}$$

Where $\boldsymbol{d}$ is the critical distance, $\boldsymbol{U_I}$ is the ionization potential of the atom, $\emptyset$ is the work function of the semiconductor, $\emptyset_{\boldsymbol{s}}$ is the amount of band bending which is proportional to the penetrated field, $\boldsymbol{\chi}$ is the semiconductor's electron affinity, and $\boldsymbol{E_{vac}}$ is the vacuum energy level.

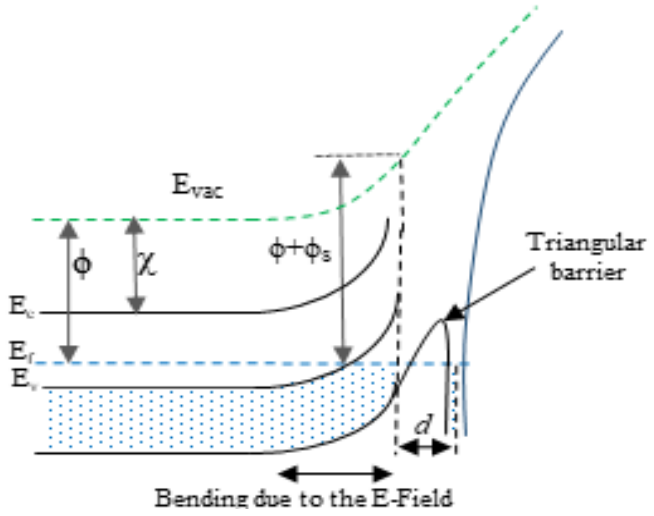

Figure 6. 1 (After Agharazy Dormeny et al. [2]) **"**Deformation of the atomic potential due to enhanced electric field at the vicinity of nanowires tips."

In this work, the electrodeposition method was used to fabricate p-type ZnO nanostructures on different substrates. Fabricated nanostructures are implemented as the anode in GIS, and the structure of the device and its performance are discussed. It was observed that the high aspect ratio flower-like nanostructures of Ag-doped ZnO grown on gold substrates can result in the largest enhancement factor among the structures discussed in this study.

6.2 Experimental Setup

6.2.1 Fabrication of Nanowires

A three-electrode electrochemical cell setup was used to fabricate ZnO nanowires. This setup is made of up the substrate as the working electrode, platinum wire gauze as the auxiliary electrode, and a saturated Ag/AgCl reference electrode. The potentiostatic mode with applying a constant cathodic voltage to the working electrode was used to perform the electro-deposition of the nanostructures. P-type (100) silicon (with resistivity between 5-10 Ω.cm) and gold-coated

silicon wafers (Si wafer with 500 μm thickness coated with 1000 Å gold, Sigma-Aldrich) were used as substrates, and they were cut in 2 × 2 cm^2 pieces. Isopropyl alcohol was used to clean gold-coated substrates, and p-type Si wafers were cleaned by the RCA technique. In order to make the electrolyte, 5.4 mM solution with an equal amount of zinc nitrate hexahydrate, $Zn(NO_3)_2.6H_2O$ (Fisher Chemical), and hexamethylenetetramine, $C_6H_{12}N_4$, (Alfa Aesar) was used.

0.026 mM of silver nitrate, $AgNO_3$ (Fisher Scientific), was added to the electrolyte to produce p-type ZnO semiconductor [67]. The process was then continued by 20 minutes of stirring the solution at a constant temperature of 75 °C (using an oil bath). The concentration of the electrolyte was kept constant using a condenser during the experiment.

Substrate material, duration of the deposition, temperature, applied voltage, and concentration of the electrolyte are the main parameters affecting the morphology of the synthesized nanostructures. These parameters and their effect on the resulting morphology of the nanostructures are investigated in the previous studies [68]. It was observed that for fabricating uniform arrays of nanowires on the substrate, a cathodic voltage of 1 volt is required to be applied on the substrate during the growth process. In order to provide an appropriate growth rate, the temperature of the electrolyte was kept constant at 75 °C throughout the growth process. Increasing the temperate results in the growth of thicker nanowires which are not suitable for gas sensing applications. For both substrates (Au and Si), the growth process time was varied between 60, 120, and 180 minutes. Hereafter, these samples are referred to as Au-60, Au-120, Au-180, Si-60, Si-120, and Si-180, respectively.

To investigate the elemental analysis of the grown nanostructures, Energy-dispersive X-ray spectroscopy (EDXS) was used. Figure 6.2 depicts the results of the element analysis for p-type

ZnO (silver doped ZnO nanowires). As shown in figure 6.2.a-c, the distribution of O_2, Zn, and Ag elements is almost uniform over the fabricated structures. In addition, as shown in figure 6.2.e, the EDXS spectrum shows the existence of 0.65 atomic% of Ag dopants in the structure.

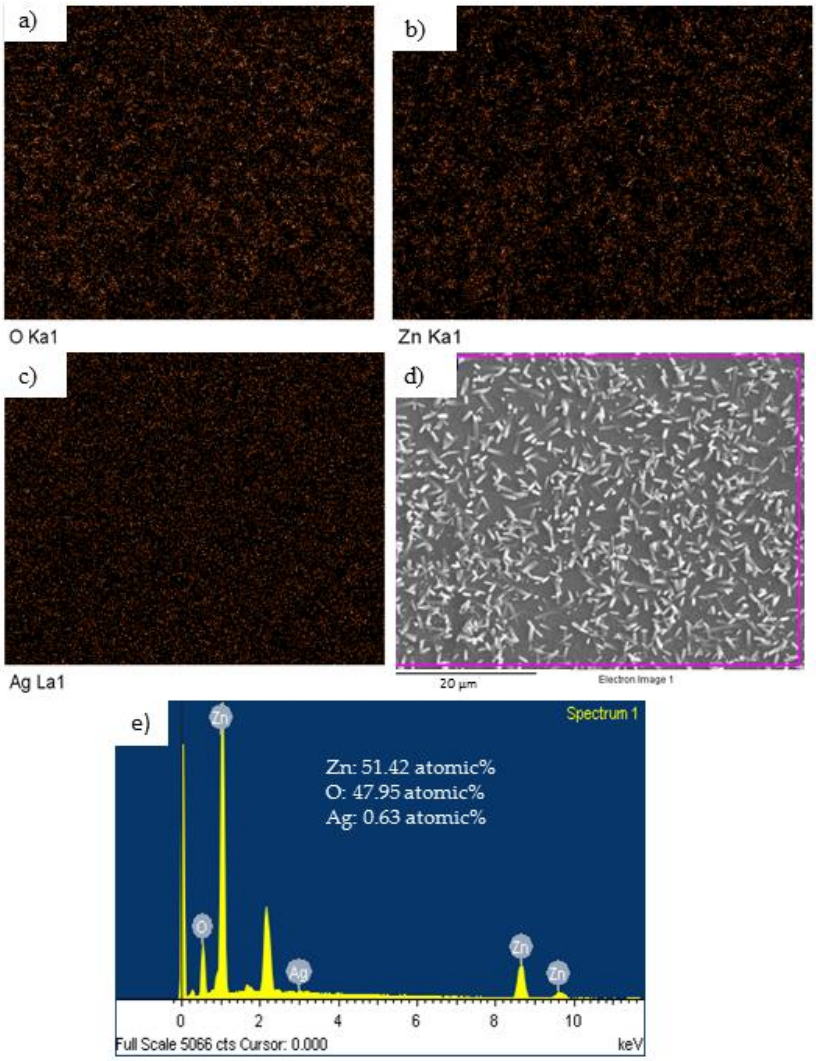

Figure 6. 2 (After Agharazy Dormeny et al. [2]) **"**EDXS and mapping analysis of fabricated Ag-doped ZnO NWs. a) Distribution of oxygen, b) Distribution of Zinc, c) Distribution of Silver dopants, d) Studied site, e) Spectrum analysis shows 51.42 atomic% Zn, 47.93 atomic% O and 0.65 atomic% Ag."

The transmission electron microscope (TEM) images and elemental analysis of individual nanowires from samples Au-180 and Si-60 are shown in figure 6.3. By comparing figure 6.3.a and 6.3.b, it can be observed that due to the growth process time, the dimensions of Si-60 sample (Figure 6.3.a) is less than Au-180 (Figure 6.3.b). The tips of the nanowires, size, and distribution of silver nanoparticles over ZnO nanowires are shown in the insets of the figures. The EDXS results of both samples are shown in figure 6.3.c, which confirms the existence of silver in the structures.

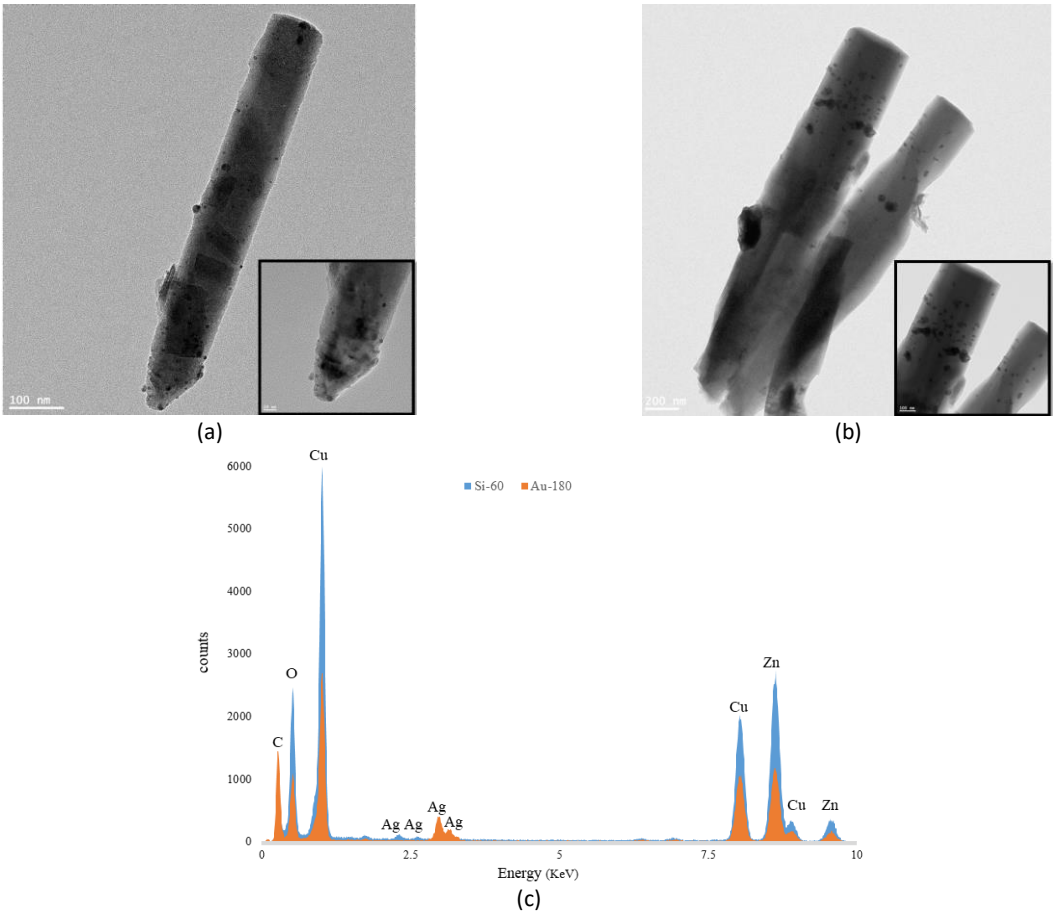

Figure 6. 3 (After Agharazy Dormeny et al. [2]) **"**TEM analysis of individual nanowires. a) Nanowire from Si-60 specimen. b) Nanowire from Au-180 specimen. c) Elemental analysis from the areas shown in the insets of the pictures. The existence of Copper and Carbon in the resulting spectra is due to the TEM grid used for the analysis. (The data is collected on FEI Tecnai 200 kV

Cryo-STEM microscope located at the Facility for Electron Microscopy Research at McGill University.)"

6.2.2 Fabrication of Gas Sensor

Figure 6.4 depicts the structure of the gas sensor schematically. The anode of the sensor consists of the fabricated ZnO nanowires, and the cathode is made of aluminum-coated Si wafer. A high-temperature resistant double-sided tape with a thickness of 100 µm was used to separate the electrodes. The sensor was then placed in a gas chamber. Before inserting any gas inside the chamber, the chamber was vacuumed to 10^{-5} Torr. Then, each gas was introduced and the I-V characteristic of the sensor was obtained for each gas using HP4155 parameter analyzer. In this study, the device was tested for Argon (Ar), Nitrogen (N_2), and Helium (He) gasses under low pressures (10^{-2} Torr). To obtain the I-V curve, the voltage was swept between 0 V to 100 V with steps of 0.5 V and a delay of 1 second.

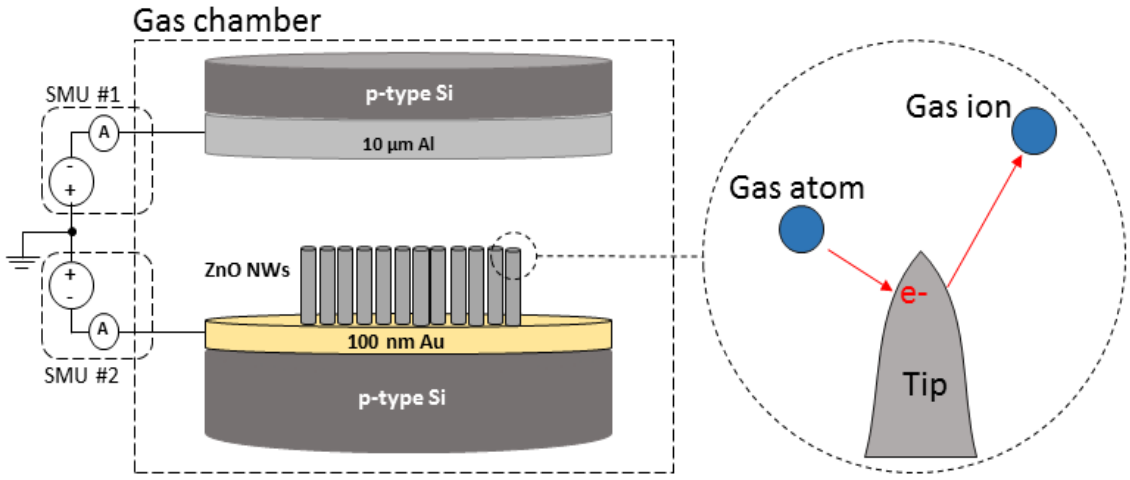

Figure 6. 4 (After Agharazy Dormeny et al. [2]) **"**Schematic of the gas sensor. The figure in the magnified section represents the tip of a nanowire and the tunneling of the valence electron of the gas into the anode and repelling the positive ion toward the cathode. The carriers will be

neutralized through the external circuit shown in the schematics and the current of SMUs are being recorded."

6.3 Results and Discussion

6.3.1 Enhancement Factor

When a voltage difference is applied between the two parallel plates, a uniform electric field is generated, which is known as the applied macroscopic field and is defined as:

$$E_{app} = \frac{V}{d} \tag{18}$$

Where V is the applied potential, and d is the distance between the parallel plates. By implementing one-dimensional nanowires on one of the electrodes, a nonlinear electric field E_{loc}, at the vicinity of the tips of the structures is generated, which has a larger magnitude than the applied macroscopic field [69]. The field enhancement factor is defined as the ratio of E_{loc} to E_{app}:

$$\beta = \frac{E_{loc}}{E_{app}} \tag{19}$$

The performance of the GIS sensors is highly dependent on the field enhancement factor. By increasing the local electric field at the tip of the nanowires, the field enhancement factor increases. This increase in the value of β intensifies the rate of the gas ionization, and consequently, reduces the breakdown voltage of the sensor. To calculate the field enhancement factor, various analytical studies have been previously reported [69], [70]. However, in all these studies, β can only be calculated for one single nanowire. In a GIS structure, there are thousands of nanowires that can affect the electric field distribution and magnification. As a result, to optimize the design and structure of the device, it is required to know the average field enhancement factor of the whole structure, $\beta_{tol.}$ However, due to the different constructive and

destructive interferences of the induced electric field at the tip of the nanostructures, and a large number of nanowires, Analytical calculation of β_{tol} is a non-trivial task. Estimation of β_{tol} can be done using the slope of the gas discharge graph (I-V curves) in the ohmic region of the curves. The discharge characteristics of gasses in a GIS with parallel electrodes (uniform electric field) are shown in figure 6.5. Due to the ionization of the gas atoms by cosmic radiation, each gas has positive ions and free-floating negative electrons. In the ohmic region, as a voltage difference is applied to the parallel electrodes, electrons start migrating to the anode and the positive ions migrate to the cathode. This migration is due to the current generated by the traveling radiation-generated charged particles. In this region, as the applied voltage increases (as the electric field magnification increases), the induced current gets amplified. By increasing the voltage, the current gets saturated (in the saturated region). This means that all radiation-generated particles are attracting to the electrodes. In the Townsend discharge region, as the applied voltage increases, the current raises exponentially. At this stage, the amplitude of the electric field is high enough to result in the acceleration of the electrons and ionizing collisions. Finally, when the electric field magnitude is large, breakdown occurs. At this voltage (V_b), the discharge can be maintained only by the ionizing collisions without any external ionization source [62].

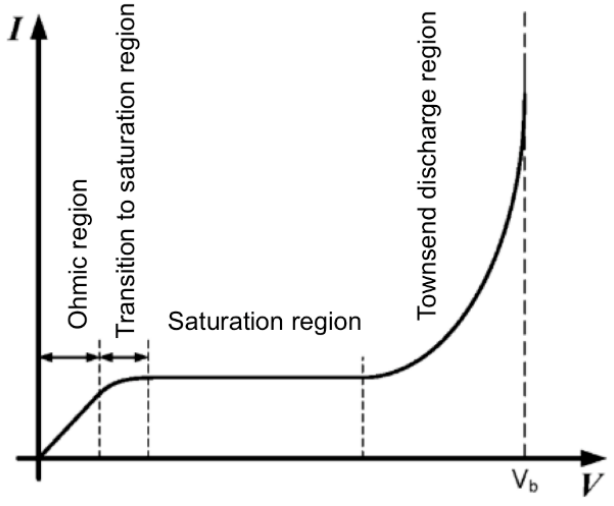

Figure 6. 5 (After Agharazy Dormeny et al. [2]) **"**Discharge characteristics in uniform fields between the parallel plates."

Since there is an almost linear characteristic between the current and voltage in the ohmic region of the I-V curves, all the β factor investigations have been done in this region. Figure 6.6 shows the I-V curves of the parallel plate capacitor (PPL) and fabricated sensors in their ohmic region under vacuum conditions (10^{-5} Torr). To estimate β_{tol}, the slope of each curve in the ohmic region was calculated and divided by the slope of the PPL device as

$$\beta_{tol} = \frac{\text{Slope}_{\text{Device}}}{\text{Slope}_{\text{PPL}}} \tag{20}$$

Another important parameter about the physical phenomena inside GIS shown in figure 6.6 is about the difference between the GIBS and GFITS based on the curvature of the graphs. As can be seen in the figure, for the PPL device, the I-V curve moves downward as the applied voltage is increased, indicating the transition from ohmic region to saturation region (refer to figure 6.5). However, for the other devices, the I-V curves (GFITS based on nanowires), the curves move upward, which shows the transition from ohmic region to tunneling region, which is discussed in the next section.

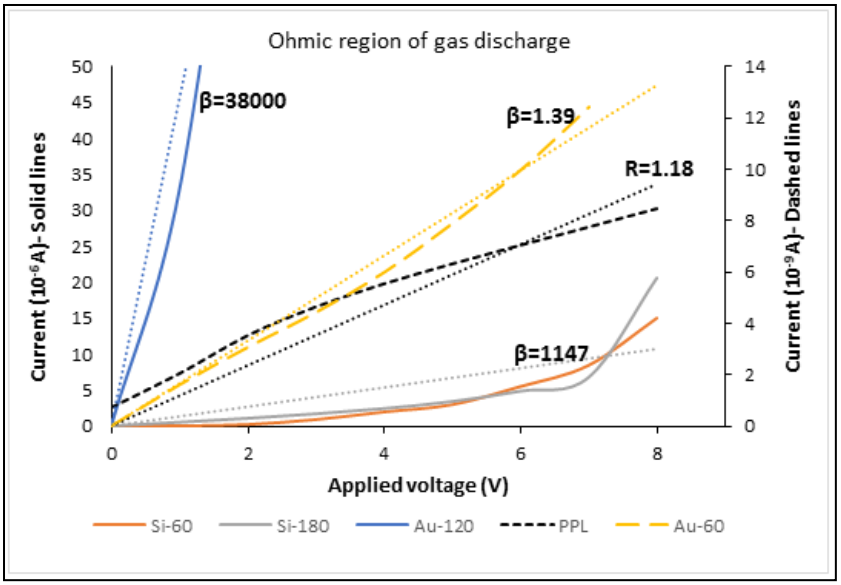

Figure 6. 6 (After Agharazy Dormeny et al. [2]) **"**Estimated **e**nhancement factor (β_{tol}) generated by nanostructures in the fabricated devices. Left vertical axis corresponds to solid lines showing the enhancement factor of the devices made by Au-120, Si-60 and Si-180. Right vertical axis corresponds to those of made by Au-60 and PPL. Trend lines show the slope of each curve. The slope of PPL graph is shown by "R", which is used as a reference to calculate β_{tol} of the nanowires."

6.3.2 Characterization of the Gas Sensors

To investigate the I-V characteristics and the breakdown voltages of different gasses, two types of vertically-aligned and flower-shaped nanostructures are implemented as the anode of GIS, and the performance of the sensors for different gasses are studied.

6.3.2.1 Vertically-aligned Nanowires

Considering the curves of Si-60 and Si-180 devices in figure 6.6, it can be concluded that since the enhancement factor for both sensors is almost the same ($\beta \approx 1000$), increasing the time of the fabrication does not have any significant effect on the field-enhancement property of nanowires. The SEM images shown in figure 6.7.a (for Si-60 device) and 6.7.b (for Si-180 device) confirm these observations. As shown in the figures, by increasing the duration of the

growth process, just the density of the nanowires has been increased, and the aspect ratios of the structures are almost the same. It is worth mentioning that due to the interference of the electric fields at the tips of the nanostructures, the higher density of the nanowires may not necessarily increase the β factor [70].

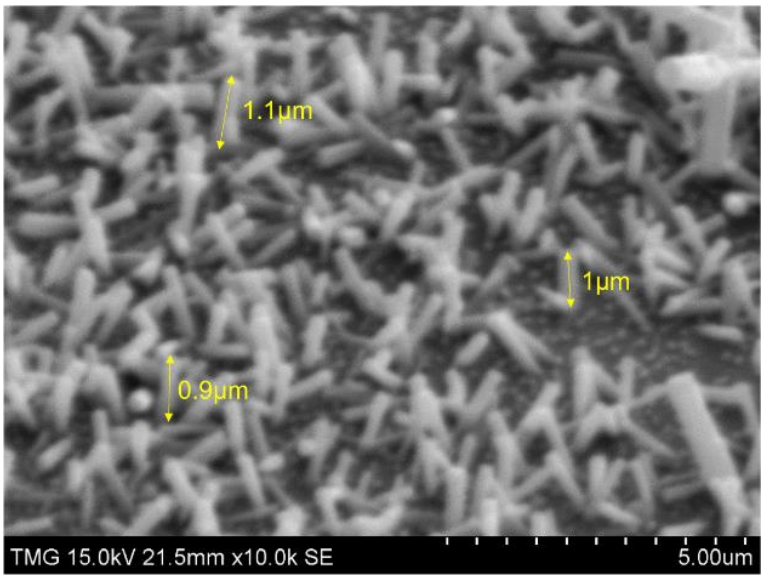

(a)

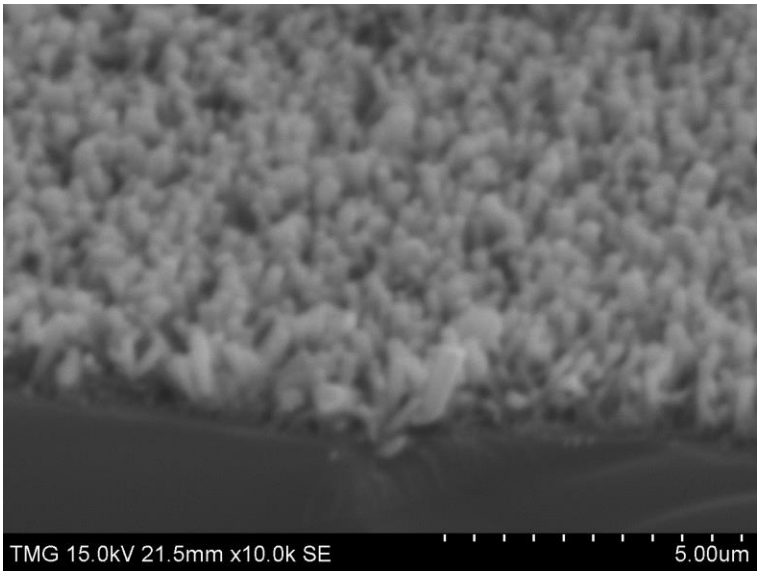

(b)

Figure 6. 7 (After Agharazy Dormeny et al. [2]) **"**a) SEM image of Si-60 ZnO nanowires shows the average length of 1 μm. b) SEM image of Si-180 nanowires shows approximately the same average length as of Si-60."

The field ionization curves of the sensor made up of Si-60 as the anode are shown in figure 6.8. The test has been performed at room temperature for He, N_2, and Ar at the pressure of 10^{-2} Torr. The transition from the ohmic region to the tunneling region is clearly shown in the figure. In the tunneling region, the current increases very rapidly with respect to the applied voltage. The sudden rises in the current at a voltage between 50 to 60 volts are called "quasi-breakdown". At the quasi-breakdown voltage, the magnitude of the electric field is so high that all the gas molecules approaching the tips of the nanostructures become ionized. Due to this reason, at this voltage, many ions are generated and the quantity of the positive ions on the cathode electrode increases. As a result, an internal electric field in the opposite direction to the applied field is generated, which reduces the total electric field inside the chamber and slows down the field ionization rate.

Our observations showed that, as expected, Si-60 and Si-180 devices show similar tunneling currents and quasi-breakdown voltages. The reason for this phenomenon is the similarity in the field enhancement factor of these sensors (figure 6.6). The effect of the gas pressure on the breakdown voltage of the sensor made up of Si-60 sample is illustrated in figure 6.9. For this test, helium gas with pressures of 0.01, 0.1, and 1 Torr is used. As clearly shown in the figure, by increasing the pressure of the gas, the breakdown voltage is increased, and the sensor can differentiate between various pressures.

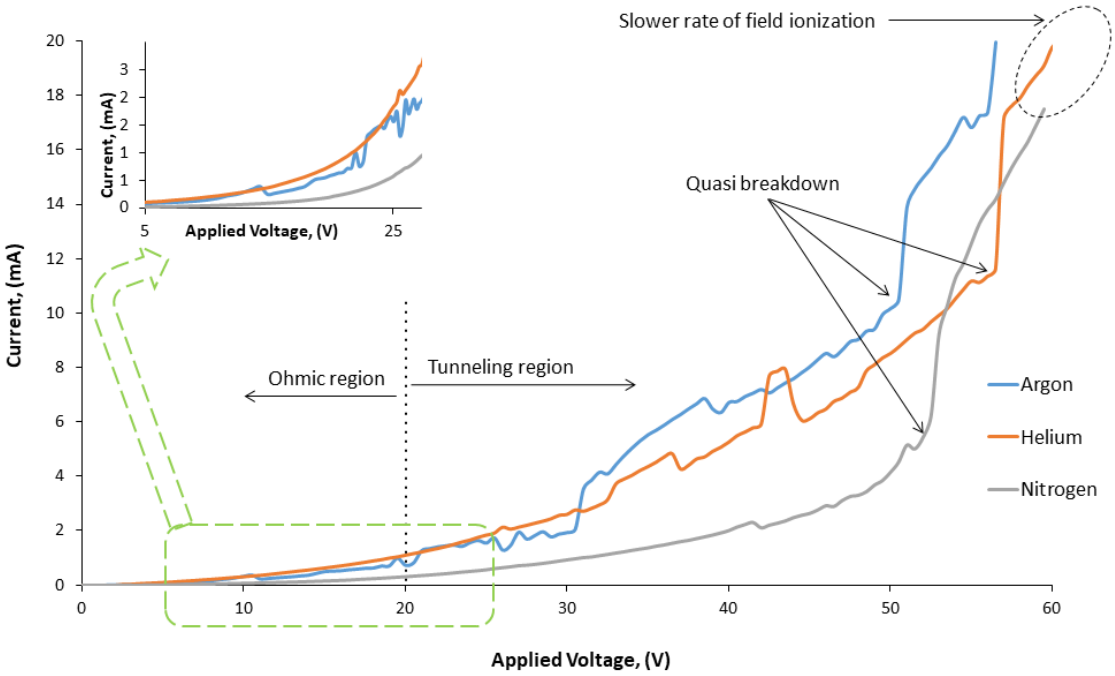

Figure 6. 8 (After Agharazy Dormeny et al. [2]) **"**Field ionization (I-V) graphs for the sensor fabricated with Si-60 sample. Approximately above 20 volts, the current increases steeply which can be defined as the tunneling region. The curves also show quasi-breakdown voltages that can be used as calibration data for the gas sensors. The transition from ohmic to tunneling region is magnified and shown in the inset."

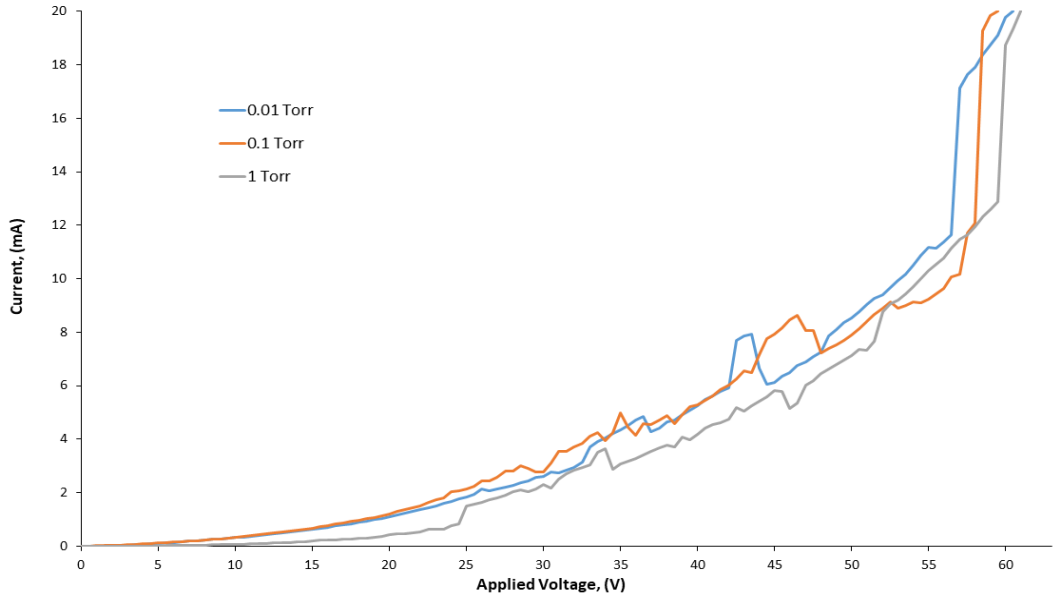

Figure 6. 9 (After Agharazy Dormeny et al. [2]) **"**I-V characteristics of the device fabricated with Si-60 sample for He under different pressures."

6.3.2.2 Flower-like Nanostructures

For the nanostructures grown on gold-coated silicon, our observations show the field enhancement factor is highly dependent on the duration of the growth process. When the duration of the experiment is 60 minutes (Au-60 device), β_{tol} was about 1.4, and it did not display field ionization currents due to the insufficient field enhancement. However, increasing the growth time to 120 minutes (Au-120 device), resulted in increasing the β_{tol} factor to around 3.8 x 10^4, and 7.62 x 10^5 for the Au-180 sample (this sample is not shown in figure 6 as its ohmic region happens to be below 0.5 volts). As the duration of the experiment was exceeding 60 minutes, "flower-like" ZnO nanostructures were forming, and the increase in the enhancement factor can be attributed to the formation of these structures. The SEM images of Au-120 and Au-180 devices are shown in figure 6.10.a and 6.10.b, respectively. The repeated growth of 2D ZnO nanosheets has resulted in the formation of the flower with hexagonal shapes [71], [72].

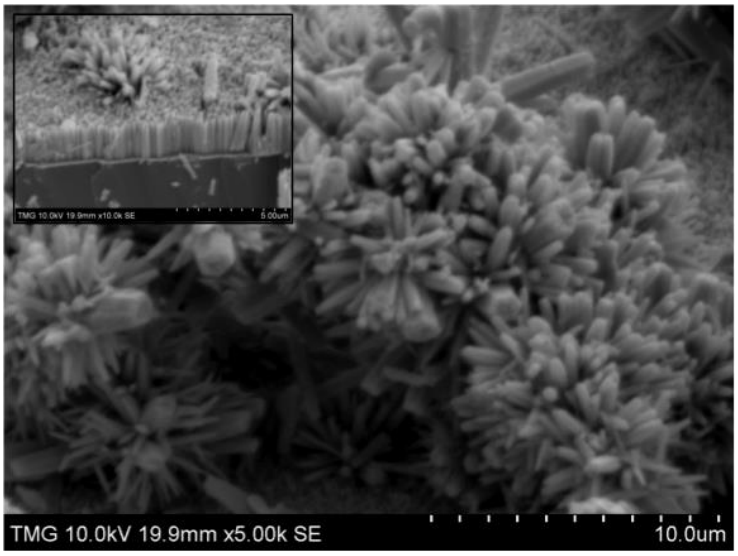

(a)

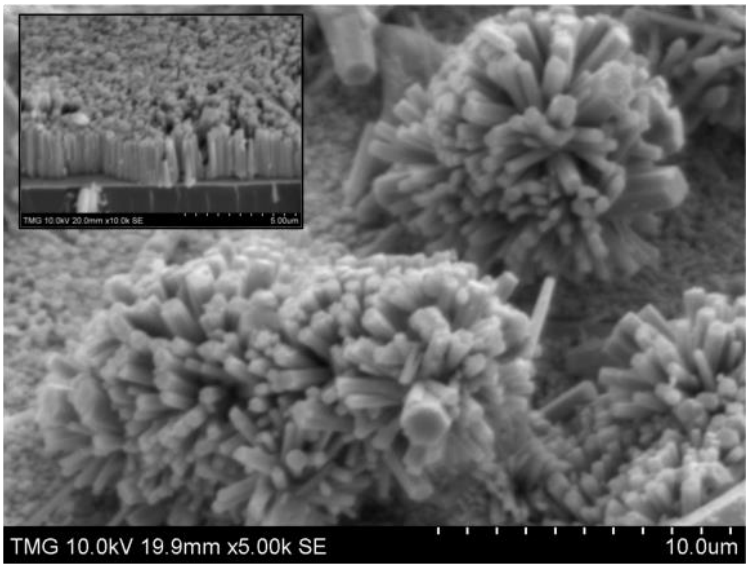

(b)

Figure 6. 10 (After Agharazy Dormeny et al. [2]) **"**SEM images of "Flower-like" structures a) Au-120 (the inset figure shows background nanowire layer with 2 μm length) b) Au-180 (the inset figure shows background nanowire layer with 2.5 μm length)."

As mentioned earlier, high aspect ratio ZnO flowers and increasing the effective surface area due to the flower-like structures are the main reasons for large field enhancement factors for Au-120 and Au-180 devices. The constructive interferences of the electric field around the flower-like nanostructures is another important parameter affecting the β_{tol} factor. These constructive interferences are due to the spherical alignment and orientation of the nanowires. Field ionization curves of the sensor made up of Au-180 sample, for He, N_2, and Ar at the pressure of 10^{-2} Torr and room temperature are shown in figure 6.11.a. Due to the very large value of the β_{tol}, the field ionization tunneling current reaches the current compliance of 30 mA within 6 volts for all three gasses. Consequently, it would be difficult to observe the changes in the tunneling current values and specifying some calibration points. As a result, for this device, the logarithmic graph was used to clearly show the transition point from the ohmic region to the tunneling region. The

logarithmic I-V characteristic of this device is shown in figure 6.11.b (for the same gasses in the same condition). As can be clearly seen, the knee point, which shows the transition from the ohmic region to the tunneling region, can be used as the calibrating data for this sensor.

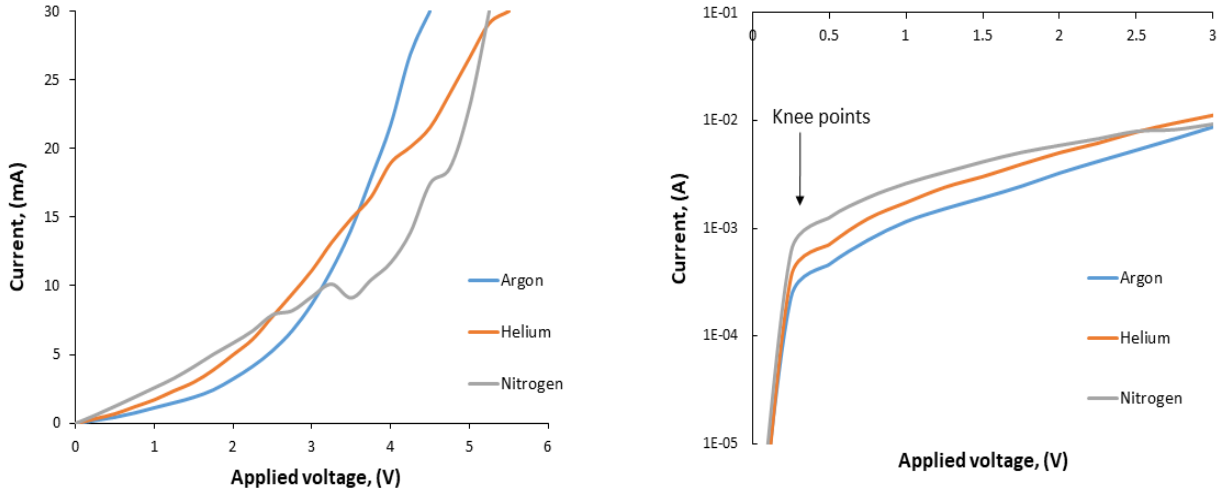

(a) (b)

Figure 6. 11 (After Agharazy Dormeny et al. [2]) "a) I-V characteristics of the device made by Au-180 for Ar, He, N_2 at 10^{-2} Torr. b) Log I vs V of the device. The knee point is used to calibrate the devices."

6.3.2.3 Numerical Simulations of the Field Enhancement Factor

As mentioned previously, there are two main reasons responsible for the large enhancement factor of the flower-like ZnO nanostructures. First, in flower-shaped structures, most of the nano-rods are emanated from the center, which amplifies the electric field in several steps [73]. As a result of this type of geometry, at the tip of the flower-like nanostructures, the electric field gets more magnification compared to those with arrays of parallel nanowires. Secondly, when the nanowires are grown very closely, the interference of induced electric fields at the tip of the nanostructures will usually reduce the effective electric field [70]. As shown in figure 6.10, since the distance between the tips of the nanowires in flower-like structures is much larger than those

of vertically aligned nanowires, destructive interferences become much smaller in flower-shaped nanostructures.

To study the effect of shape of the nanostructure on the electric field magnitude in GIS, models were developed to compare the field enhancement in flower-like nanostructures with those of vertically aligned nanostructures. In these models, we have just considered the general shape of the nanostructures, and small protrusions or whiskers on the surface of the structures are neglected.

To simulate the sensors, two devices with the same parameters used in practice (vertically aligned and flower-like ZnO nanostructures) were modeled in COMSOL Multiphysics (electrostatics module), and electric field inside each device was measured. The geometry of the model, containing two parallel silicon plates as cathode and anode in the Argon environment and ZnO nanostructures on the anode, is demonstrated in figure 6.12.a. To induce an electric field, a voltage of 55 volts was applied between the electrodes and the local electric fields generated between the plates, and at the tips of the vertically aligned and flower-like nanowires are shown in figure 6.12.b and 6.12.c, respectively. By comparing these figures, it can be observed that the maximum electric field in vertically aligned nanowires is equal to 1.31 x 10^7 Vm^{-1}. While the maximum field observed in flower-shaped nanostructures for the same applied voltage is 7.79 × 10^7 Vm^{-1} (around 6 times higher). The analytical results are in good agreement with what we observed in the experimental results.

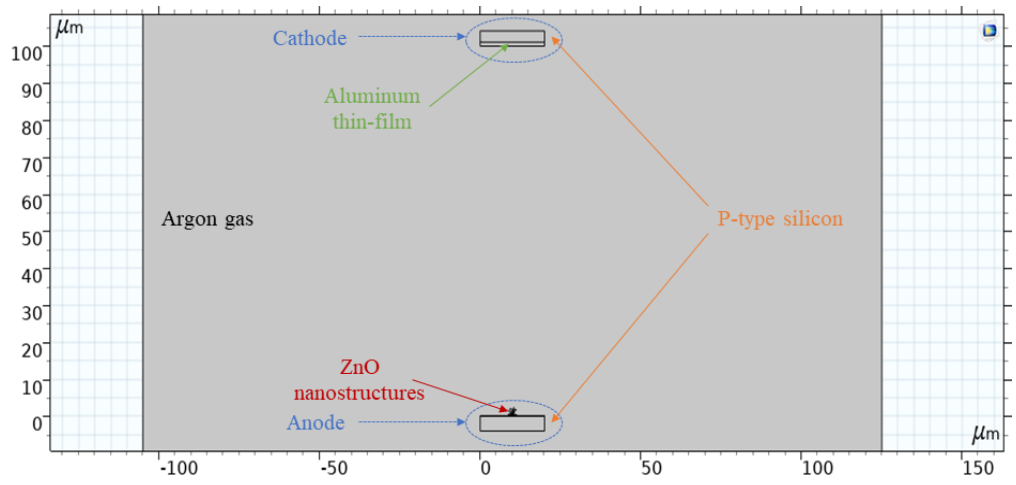
μm
Cathode
Aluminum
thin-film
Argon gas
P-type silicon
ZnO
nanostructures
Anode
μm

(a)

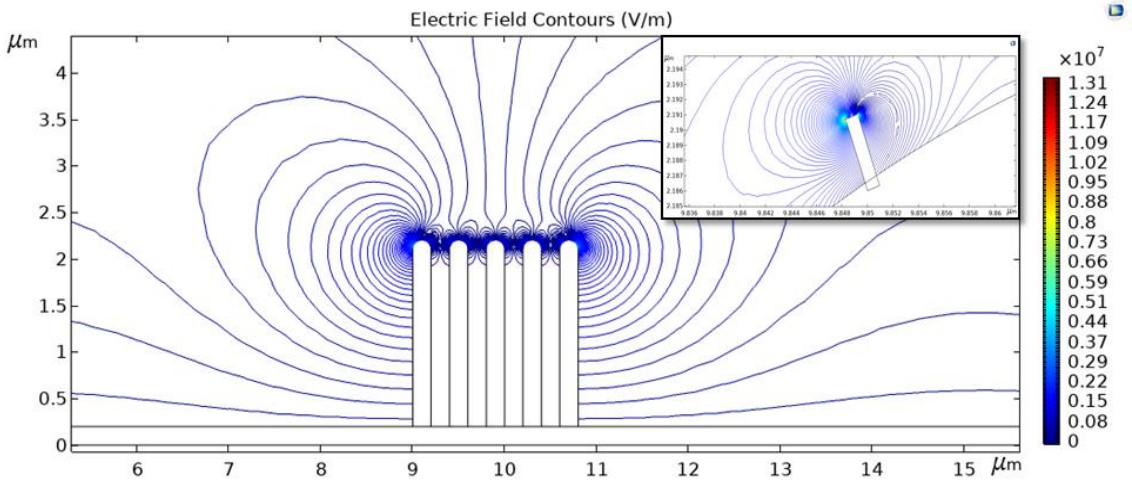
Electric Field Contours (V/m)
μm
×10^7
1.31
1.24
1.17
1.09
1.02
0.95
0.88
0.8
0.73
0.66
0.59
0.51
0.44
0.37
0.29
0.22
0.15
0.08
0
μm

(b)

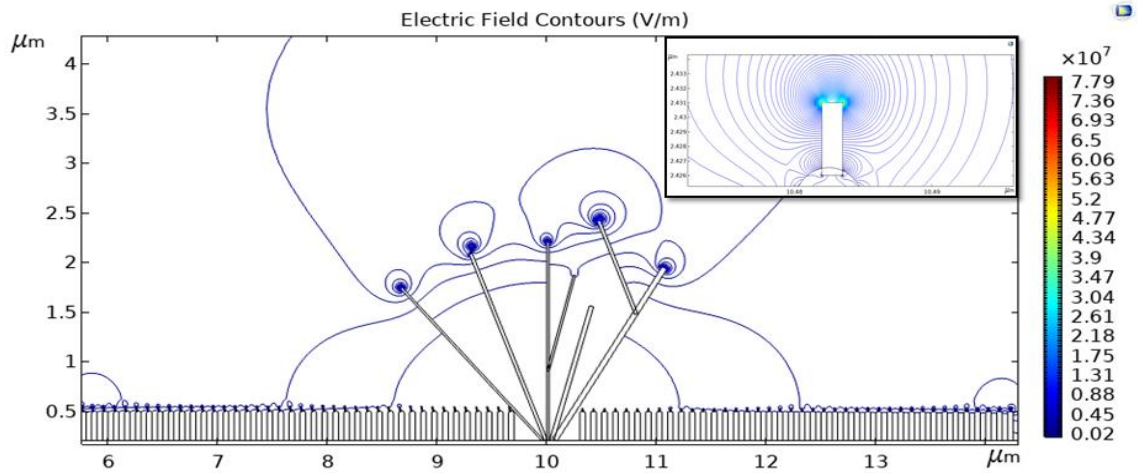
Electric Field Contours (V/m)
μm
×10^7
7.79
7.36
6.93
6.5
6.06
5.63
5.2
4.77
4.34
3.9
3.47
3.04
2.61
2.18
1.75
1.31
0.88
0.45
0.02
μm

(c)

Figure 6. 12 (After Agharazy Dormeny et al. [2]) **"**a) Geometry of the designed model. b) Electric field contours generated around the tips of the free-standing nanowires. c) Electric field contours generated around the tips of the flower-like nanostructures. The insets in figure 6.12.b and 6.12.c show the tip of the nanostructures where the electric field is maximum."

6.4 Conclusions

In this chapter, the growth of the ZnO nanowires on p-type silicon and gold-coated silicon substrates using the electrochemical deposition technique was explained. The fabricated nanostructures were applied as the anode of a miniaturized GFITS, and the device was used to detect N_2, Ar, and He gasses under low pressures. For the devices made from p-type silicon substrates (Si-60 and Si-180), the results showed that the tunneling current starts at around 20 V, and a quasi-breakdown between 50-57 V can be observed for all the target gasses, which can be used as calibrating data for these structures.

For the devices made from gold-coated silicon substrates, the ZnO nanostructures had flower-shaped morphologies, and as a result, these devices showed the lowest onset voltages. In these devices, by applying 0.5 V, the field ionization current starts, and it reaches the 30 mA compliance current at voltages between 3 to 5 volts (depending on the target gas). The numerical simulations in COMSOL demonstrated that the amplification of the local electric field in flower-like nanostructures is much larger than that of vertically aligned nanowires, which is consistent with the experimental observations.